ELSEVIER

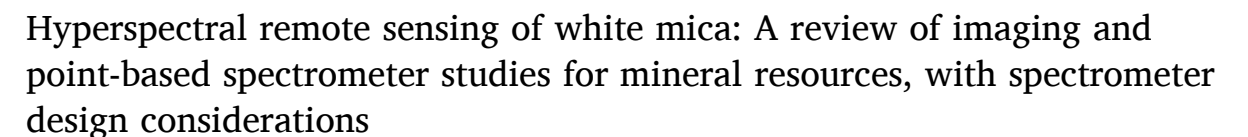
Contents lists available at ScienceDirect

Remote Sensing of Environment

journal homepage: www.elsevier.com/locate/rse



Review





John M. Meyer a,b,*, Raymond F. Kokaly a, Elizabeth Holley b

- ^a United States Geological Survey, Box 25046, MS 973, Denver, CO 80225-0046, USA
- b Department of Mining Engineering, Colorado School of Mines, 1600 Illinois Street, Golden, CO 80401, USA

ARTICLEINFO

Editor: Jing M. Chen

Keywords: Imaging spectroscopy White mica Mineral occurrences Spectrometer design Geo-spectral deposit model

ABSTRACT

Over the past \sim 30 years, hyperspectral remote sensing of chemical variations in white mica have proven to be useful for ore deposit studies in a range of deposit types. To better understand mineral deposits and to guide spectrometer design, this contrib ution reviews relevant papers from the fields of remote sensing, spectroscopy, and geology that have utilized spectral changes caused by chemical variation in white micas. This contribution reviews spectral studies conducted at the following types of mineral deposits: base metal sulfide, epithermal, porphyry, sedimentary rock hosted gold deposits, orogenic gold, iron oxide copper gold, and unconformity-related uranium. The structure, chemical composition, and spectral features of white micas, in this contribution defined as muscovite, paragonite, celadonite, phengite, illite, and sericite, are given. Reviewed laboratory spectral studies determined that shifts in the position of the white mica 2200 nm combination feature of 1 nm correspond to a change in Al^{oct} content of approximately $\pm 1.05\%$. Many of the reviewed spectral studies indicated that a shift in the position of the white mica 2200 nm combination feature of 1 nm was geologically significant.

A sensitivity analysis of spectrometer characteristics; bandpass, sampling interval, and channel position, is conducted using spectra of 19 white micas with deep absorption features to determine minimum characteristics required to accurately measure a shift in the position of the white mica 2200 nm combination feature. It was determined that a sampling interval < 16.3 nm and bandpass < 17.5 nm are needed to achieve a root mean square error (RMSE) of 2 nm, whereas a sampling interval < 8.8 nm and bandpass < 9.8 nm are needed to achieve a RMSE of 1 nm. For comparison, commonly used imaging spectrometers HyMap, AVIRIS-Classic, SpecTIR®'s AisaFENIX 1K, and HySpex MIR 384 have 2.1, 1.2, 0.96, and 0.95 nm RMSE in determining the position of the 2200 nm white mica combination feature, respectively.

An additional sensitivity analysis is conducted to determine the effect of signal to noise ratio (SNR) on the RMSE of the position of the white mica 2200 nm combination feature, using spectra of 18 white micas with deep absorption features. For a spectrometer with sampling interval and bandpass of 1 nm, we estimate that RMSEs of 1 and 1.5 nm are achievable with spectra having a minimum SNR of approximately 246 and 64, respectively. For a spectrometer with sampling interval and bandpass of 5 nm, we estimate that RMSEs of 1 and 1.5 nm are attainable with spectra having a minimum SNR of approximately 431 and 84, respectively. When using a spectrometer with a sampling interval 8.8 nm and a bandpass of 9.8 nm, a RMSE of 1 is only achievable with convolved, noiseless reference spectra. For the 8.8_9.8 nm spectrometer, spectra with SNR of 250 and 100 result in RMSE of 1.1 and 1.3, respectively. Therefore, fine spectral resolution characteristics achieve RMSEs better than 1 nm for high SNR spectra while spectrometers with coarse spectral resolution have larger RMSE, perform well with noisy data, and are useful for white mica studies if RMSE of 1.1 to 1.5 nm is acceptable.

^{*} Corresponding author at: United States Geological Survey, Box 25046, MS 973, Denver, CO 80225-0046, USA. *E-mail address*: jmmeyer@usgs.gov (J.M. Meyer).

1. Introduction

The majority of ore deposits are the result of, or have been significantly modified by, the circulation of hot aqueous fluids in the Earth's crust (Franklin et al., 2005; Groves et al., 2010; Groves et al., 1998; Robb, 2004; Sillitoe, 2010; Simmons et al., 2005). Muscovite, illite, and sericite are common hydrothermal alteration products of feldspars found in ore deposits and mineralized zones. Because these minerals have been difficult to distinguish in past hyperspectral remote sensing studies, they are often grouped together and referred to as 'white mica' (Harraden et al., 2013; Kokaly et al., 2017b; van Ruitenbeek et al., 2005). Past spectral studies of mineral deposits also describe paragonite, celadonite, and phengite as 'white mica' (Herrmann et al., 2001; Jones et al., 2005). The present contribution includes all of the abovementioned minerals as belonging to the grouping of 'white micas'. Because feldspars are the most common mineral in the Earth's crust (Wedepohl, 1986), white micas, formed from weathering and hydrothermal alteration of feldspars, are widely distributed on the surface of the Earth. Past regional spectral studies in Afghanistan (Kokaly et al., 2013), and current regional multi-scale spectral studies of the Western United States (Kokaly et al., 2021) indicate that a large portion of the short-wave infrared (SWIR) signal in these areas is white micas. When generating spectral-based mineral maps using SWIR airborne data, it is common that approximately 50% of the pixels that map as minerals are identified as white micas.

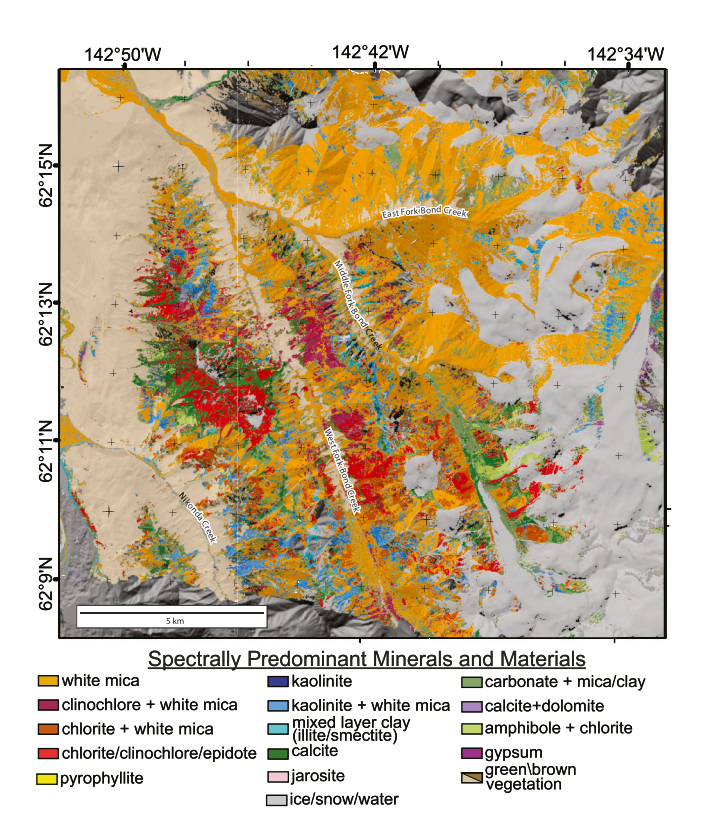
The focus of this contribution is the diagnostic absorption feature of white micas, which occurs at approximately 2200 nm. The precise position of this 2200 nm combination feature is controlled by the octahedral cation composition of the white mica (Duke and Lewis, 2010; Farmer, 1974; Kokaly et al., 2017b; Post and Noble, 1993; Rossman, 1984; Swayze et al., 2014). Variations in white mica chemical composition can be indicators of alteration type, alteration intensity, fluid geochemistry, and can be a proxy for metal grade (Harraden et al., 2013;

Herrmann et al., 2001; van Ruitenbeek et al., 2005). Mapping the district-scale spatial distribution of variations in the position of the white mica 2200 nm combination feature can indicate areas of interest for further exploration campaigns by identifying alteration patterns that typically are associated with specific deposit types (e.g., Kokaly et al., 2017b) (Fig. 1), thereby improving exploration efficiency. Furthermore, outcrop-scale mapping of active mine sites can reveal shifts in the position of the white mica 2200 nm combination feature which elucidate characteristics of the mineralized system (Fig. 2).

Fig. 3 illustrates variation in the position of the continuum removed 2200 nm combination feature in hyperspectral data collected at the Cripple Creek & Victor Mine in Cripple Creek, Colorado, USA. Three by three pixel spectral averages were calculated from various positions in the Cresson Pit, the locations of which are shown in Fig. 2 and the position of the combination feature was determined. More detailed methods descriptions and complete spectral data can be found in the associated USGS data release (Meyer et al., 2022).

The remote sensing of geology using multi-scale imaging spectrometers has been an active area of research since the early 1980's with the initial deployment of the Airborne Visible/Infrared Imaging Spectrometer (AVIRIS) and other aerial instruments such as HyMap, Hyperion, ALI, and ASTER (Cocks et al., 1998; Goetz et al., 1985; Green et al., 1998; Hubbard et al., 2003; Hunt and Ashley, 1979; van der Meer et al., 2012). The use of reflectance spectra data collected with imaging spectrometers to create spectral based mineralogy maps has increased in recent years as instruments, identification algorithms, and spectral libraries have been developed and improved (Clark et al., 2003; Clark and Roush, 1984; Kokaly, 2011; Kokaly et al., 2017a).

While previous spectral studies have been conducted at specific mineral deposits and districts, no review encompassing spectral studies at a variety of mineral deposits has been presented to date. Additionally, the authors are unaware of any previous contributions that aimed to draw conclusions regarding the spectral characteristics of various



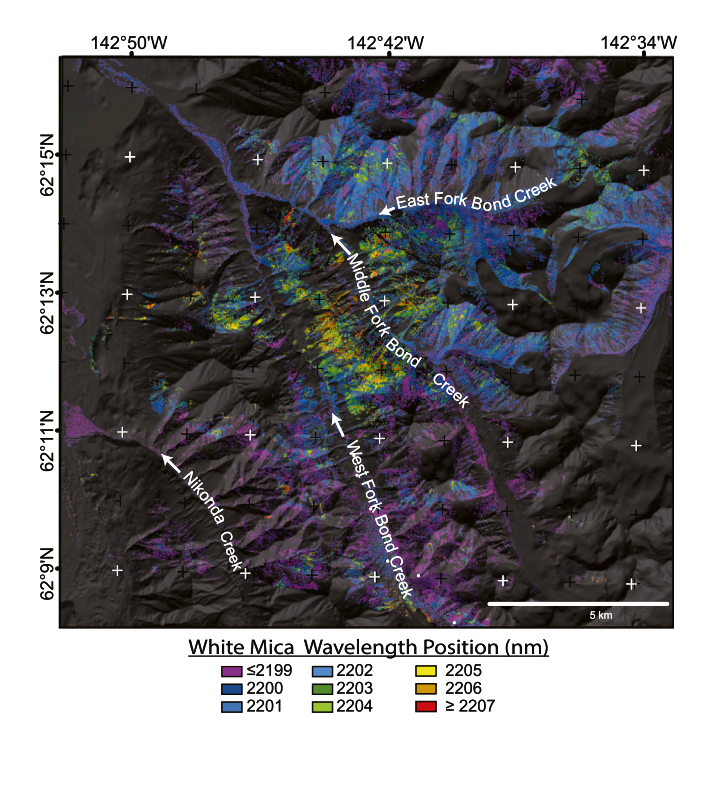


Fig. 1. District scale spectral based mineral map (on left) and white mica 2200 nm combination feature position map (on right) derived from airborne HyMap imaging spectrometer data for the Orange Hill-Bond Creek, Alaska area. White mica and white mica mixtures map over a large portion of the area. Longer wavelength white micas, indicated by warmer colors in the position map, were associated with a porphyry cluster and elevated Cu values (modified from Kokaly et al., 2017b).

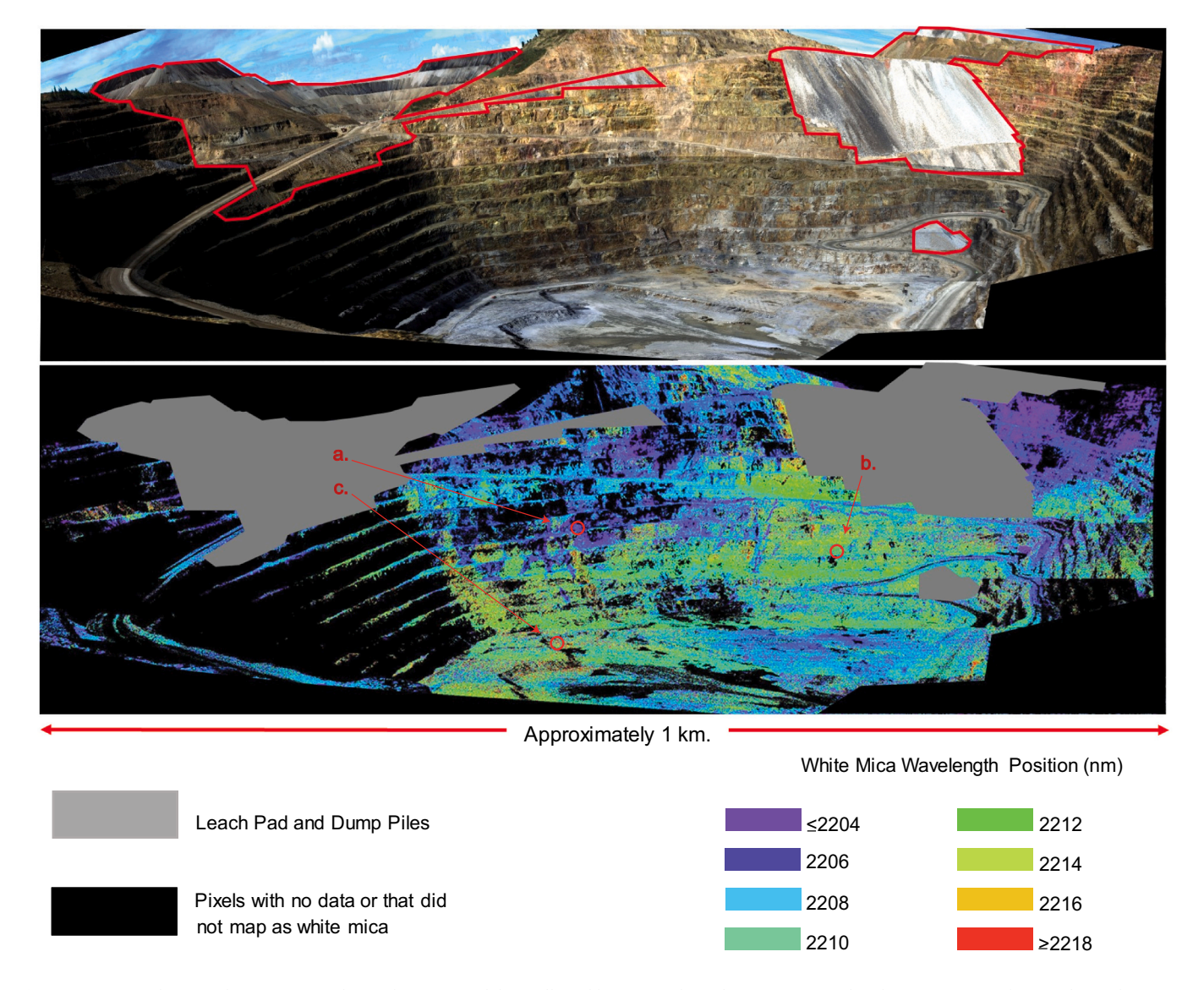


Fig. 2. Outcrop scale mineral maps generated using hyperspectral data collected by U.S. Geological Survey personnel in the Cresson Pit at the Cripple Creek & Victor Mine in Cripple Creek, Colorado, USA. Variations in the position of the white mica 2200 nm combination feature indicate variations in the chemistry, specifically the octahedral Al content, of the imaged white micas. Circles labeled a, b, and c indicate locations of 3×3 pixels averages used to generate continuum removed spectra in Fig. 3. A general trend towards longer wavelength positions (due to lower Al content in the white micas) with increasing depth in the pit corresponds to increased proximity to the Al-poor causative intrusion. The images represent a vertical cross-section of a mineralized hydrothermal system.

deposit types by means of a review and synthesis of spectral studies conducted at individual deposits. Finally, no prior studies include a sensitivity analysis of the minimum characteristics; bandpass, sampling interval, and signal to noise ratio (SNR) of a spectrometer needed to accurately record shifts in white mica parameters that may be useful in the study of mineral occurrences.

This contribution reviews the chemical composition of white micas and the relationship between the 2200 nm white mica combination feature position and mineralized zones. To accomplish this, the following section presents background information on white mica chemistry, summarizes spectral characterization of the primary SWIR absorption feature of white micas, and reviews prior work that applies shifts in the white mica wavelength position to a variety of ore deposits, mineral occurrences, and laboratory chemical composition studies. Diagnostic trends for each deposit type are identified where possible. The magnitude of the shift of the white mica wavelength position that is deemed significant by the authors of each study is noted in order to determine the characteristics of spectrometers needed to accurately measure shifts of these magnitudes. Finally, an evaluation of

spectrometer characteristics is conducted to assess the capability of different spectrometer designs to accurately define the wavelength position of the white mica 2200 nm combination absorption feature in noiseless and noisy spectra. This evaluation can help to guide instrument selection for future spectral studies of white mica.

2. Background

White micas are phyllosilicates, with a unit structure that comprises an octahedral silicate sheet (O) between two tetrahedral silicate sheets (T) with each T-O-T layer separated by planes of cations (Rieder et al., 1998). The tetrahedral sheets are made up of ${\rm SiO_4}^{4-}$ tetrahedra in sixmember rings, typically with a central hydroxyl ion (Klein et al., 2007). The octahedral sheets consist of one cation, usually ${\rm Al}^{3+}$, ${\rm Fe}^{2+}$, ${\rm Fe}^{3+}$, and ${\rm Mg}^{2+}$, bonded in octahedral coordination with six central hydroxyl ions or apical oxygens of adjacent ${\rm SiO_4}^{4-}$ tetrahedra. Substitutions of ${\rm Al}^{3+}$, Si, ${\rm Mg}^{2+}$, Fe $^{2+}$, and Fe $^{3+}$ are controlled by the Tschermak substitution (Duke, 1994):

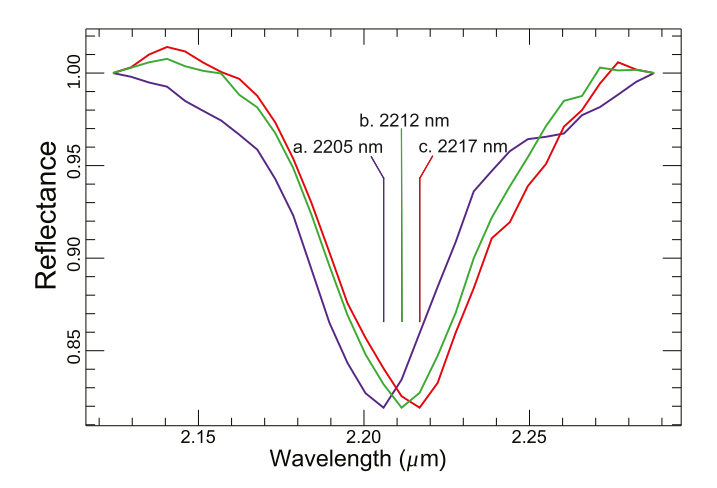


Fig. 3. Continuum removed white mica 2200 nm combination features obtained from 3×3 pixel averages in the Cripple Creek & Victor Mine hyperspectral data (Fig. 2). Spectrum 'a. 2205 nm', is scaled to match spectrums 'b.2212 nm' and 'c. 2217 nm'. A shift longward indicates a decrease in octahedral Al and corresponds to an increase in depth in the Cripple Creek & Victor Mine. See supplemental materials in Graham et al. (2018) for example spectra from Orange Hill Bond Creek, Alaska.

$$^{IV}Si + ^{VI}(Mg, Fe) \leftrightharpoons ^{IV}Al + ^{VI}Al$$

The present contribution focuses on the dioctahedral phyllosilicates muscovite, sericite, celadonite, and paragonite, as well as the illite and phengite solid solution series, as all of these have been referred to as 'white mica' in previous spectroscopy studies. See supplemental materials for discussion of white mica structure.

2.1. Formation of white mica in mineralized systems

Mineralization occurs as hydrothermal fluids transport metals from source areas until changes in temperature, pressure, or chemistry cause the solutions to precipitate their metal loads. As these hydrothermal fluids are circulating, they also interact with the surrounding wall rocks, altering the wall rock mineralogy and the chemistry of the hydrothermal fluids in predictable ways, and producing alteration products including white micas and other clays. The cause of the variation in octahedral cation content of hydrothermal white micas found in mineralized systems, and, thus, the shift in the white mica 2200 nm combination feature position, appears to be related to the geochemical properties of the causative fluids, the geochemical properties of the host rocks, and interactions between them. Temperature, salinity, and acidity of the causative fluids, along with the availability of Al, Mg, and Fe in the host rock, all appear to affect the ultimate position of the white mica 2200 nm combination feature (Cathelineau, 1988; Parry et al., 1984; Swayze et al., 2014).

3. Fundamentals of mineral spectroscopy

The reflectance spectrum of a mineral is a combination of all the aspects of that mineral that are spectrally active in the region being imaged (Hunt, 1977). Fundamental electronic processes result in absorption features in the region of approximately 300 to 1000 nm and thus can be observed directly with most spectrometers. When occurring in natural materials, these features are most commonly the result of the presence of iron (Hunt, 1977).

Fundamental vibrational processes occur when molecules in their lowest vibrational energy state, known as their ground state, absorb energy at a specific frequency, or wavelength, causing them to bend and stretch (Hunt, 1977). The energy required to transition most geologically important materials from a ground vibrational state to an excited

state falls into the mid to far infrared region. Because remote sensing instruments operate in the visible to short wave infrared region of the electromagnetic spectrum, imaging spectrometers will measure absorption features caused by overtones and combinations of these fundamental vibrations (Harris and Bertolucci, 1989; Hunt, 1977). When two or more fundamentals or overtones occur simultaneously, then a combination feature at or near the sum of the fundamental and/or overtone frequencies involved will occur (Hunt, 1977).

4. White mica reflectance spectra

The reflectance spectra of most white micas, for example muscovite (Fig. 4), are dominated by two prominent absorption features, one at approximately 1400 nm and one at approximately 2200 nm (Hunt, 1977). The 1400 nm feature will be briefly discussed here, but the focus of this contribution is on the 2200 nm feature.

The 1400 nm feature cannot be consistently resolved by imaging spectrometers in remote sensing applications due to the opacity of the Earth's atmosphere in this region caused by water vapor absorptions (Clark, 1999; Richter and Schläpfer, 2019). The 1400 nm feature can be resolved in laboratory settings and in situations where an artificial illumination source is proximal to the target. The 1400 nm feature can also be resolved when using solar illumination if post-processing steps are taken to remove atmospheric residuals. Farmer (1974) discusses of the causes of the white mica 1400 nm feature in detail.

Relative to the 1400 nm feature, the white mica 2200 nm (4545 cm⁻¹) wavelength feature can be easily resolved in remotely sensed data. The 2200 nm feature is therefore a better candidate for use in remote spectral studies and is the focus of this contribution. The 2200 nm (4545 cm⁻¹) wavelength feature is the result of a combination of the fundamental OH streching [ν (OH)] frequencies in the 3400 to 3750 ${\rm cm}^{-1}$ (~2.941 to 2.667 μm) region and the fundamental octahedral cation-OH in-plane bending modes [$\delta(OH)$] which occur in the 600 to 950 cm^{-1} (~16.667 to 10.526 $\mu m)$ region (Farmer, 1974). Shifts in either of these fundamental vibration modes will result in shifts in the position of the 2200 nm feature. While often referred to as the Al-OH absorption feature, the 2200 nm feature is a composite feature of the many cation-OH absorption features that exist in any mica. Due to the wide variation in composition of minerals referred to as 'white mica' in the spectral studies reviewed here, with the resultant contribution of many different cation-OH interactions, this feature will be referred to as the 'white mica 2200 nm combination feature' in this contribution.

4.1. OH in-plane bending mode and the 2200 nm combination feature

Variations in local composition in white micas will affect the $\delta(OH)$ frequency (Vedder, 1964). The fundamental $\delta(OH)$ features in a white mica spectrum are influenced for the most part by the makeup of its neighboring octahedral cations and occur in the mid to far infrared regions. The octahedral cation in white micas is commonly Al^{3+} , Fe^{3+} , Fe^{2+} , or Mg^{2+} (Foster, 1956; Rieder et al., 1998) thus these result in the most common cation-OH octahedral pairings. Substitutions of these cations will influence the position of both the fundamental $\nu(OH)$ and the fundamental $\delta(OH)$ frequencies (Duke, 1994; Duke and Lewis, 2010; Graham et al., 2018; Martínez-Alonso et al., 2002). A shift in the $\delta(OH)$ will lead to a corresponding shift in the 2200 nm combination feature.

4.2. OH stretching mode and the 2200 nm combination feature

The exact frequency of the $\nu(OH)$ in white micas is dependent upon the composition in the adjacent tetrahedra and octahedral sites (Farmer, 1974; Martínez-Alonso et al., 2002). Vedder (1964) determined that variation in the $\nu(OH)$ frequency in white micas was due largely to the composition and structure of the three neighboring cations in the adjacent octahedral layer, although cation substitutions in the tetrahedral layer will also shift the $\nu(OH)$ to a lesser degree (Martínez-Alonso

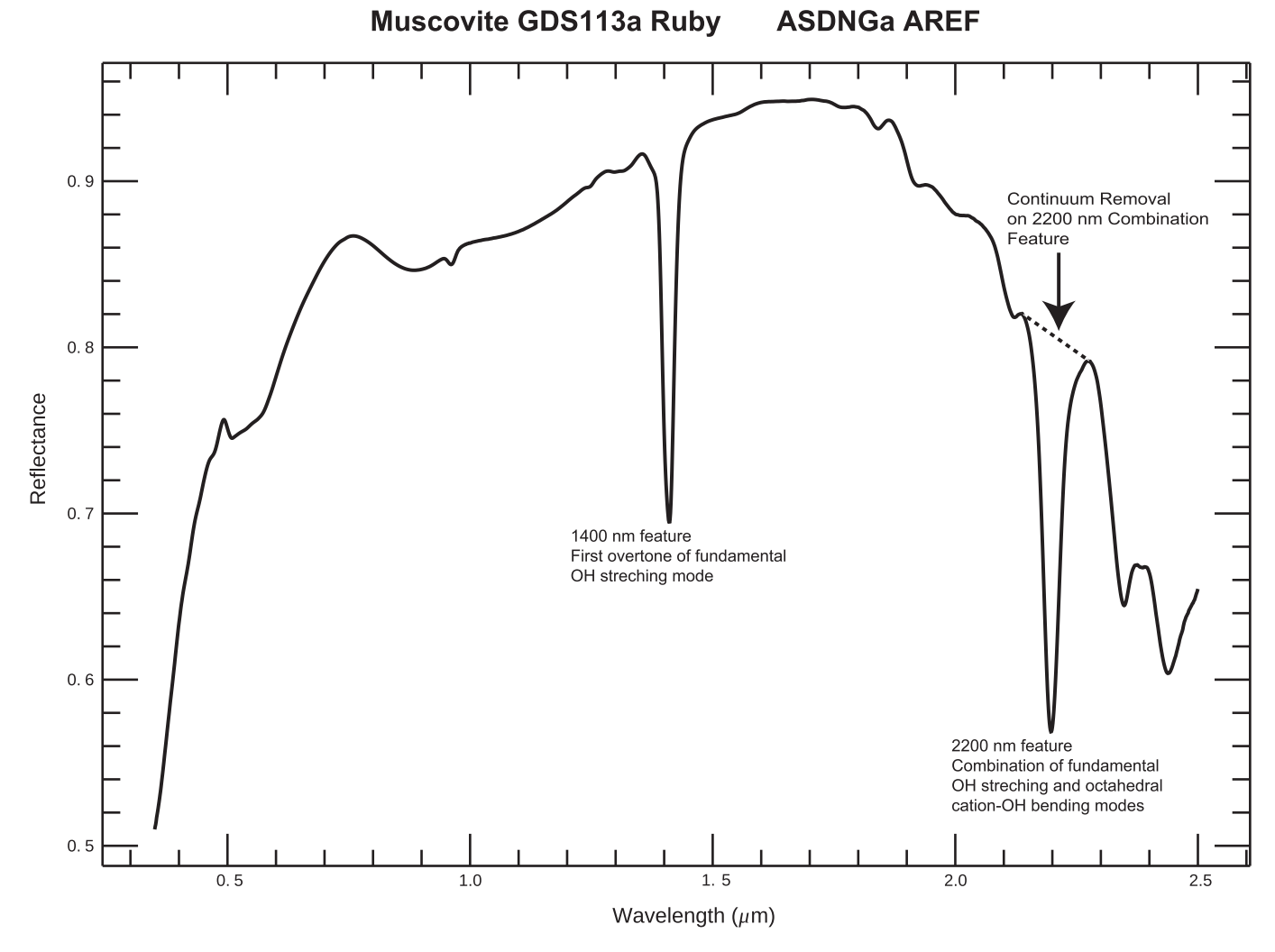


Fig. 4. Reflectance spectra of U.S. Geological Survey sample GDS 113a, a muscovite, in the region of 350–2500 nm. (Kokaly et al., 2017a). Dotted line indicates region where continuum removal is performed on the diagnostic 2200 nm combination feature in the Nicolet reference spectrum. The left continuum endpoint was set at 2142 nm and the right continuum endpoint was set at 2282 nm. The position of sample GDS 113a was determined to be 2197 nm.

et al., 2002). Substitutions of cations in the interlayer have negligible effect on the frequency of the ν (OH) (Farmer, 1974; Martínez-Alonso et al., 2002). The various environmental factors influencing the ν (OH), that is the sum of the random substitutions in the octahedral and tetrahedral layers, contribute to a broad composite absorption feature, with a FWHM of approximately 50 cm $^{-1}$ (Farmer, 1974). As is the case with the δ (OH), any shift in the position of this fundamental ν (OH) will contribute to a corresponding shift in the 2200 nm combination feature.

4.3. Combination OH stretching and OH bending feature

The position of the 2200 nm combination feature for the minerals described as 'white micas' in the studies reviewed during this contribution ranged from 2190 to 2370 nm (Bishop et al., 2008; Martínez-Alonso et al., 2002), with 51 different mineral names used to describe 'white mica'. The lack of consistent mineral naming and the wide range of white mica 2200 nm combination feature positions assigned to the various mineral names precludes a systematic review of the expected spectral features of specific compositions of white micas.

5. Review of white mica spectral studies

The following section summarizes 41 white mica field and laboratory spectral studies of ore deposits, mineral occurrences, and ore deposit-

hosting regions. The goal was to determine the magnitude of shift in the position of the 2200 nm white mica combination feature that was considered significant by the authors of the study. The smallest shift documented in these studies was 1 nm, and this determination was then used to guide the spectrometer sensitivity analysis. The terminology used when discussing the following spectral studies is that of the original authors of that study, including mineral names, deposit type, and naming of the white mica 2200 nm combination feature. The determination of a significant shift is based on the precision of shifts reported by the authors of the original studies. For example, a study that mapped white mica by wavelength position in bins of 2201 to 2205 nm, 2206 to 2210 nm, etc. would be reported in this contribution as a study having a significant shift of 5 nm. A detailed summary of the reviewed spectral studies is given in the accompanying supplemental materials.

5.1. Laboratory studies

The results of the nine laboratory studies conducted as stand-alone investigations or in conjunction with larger spectral studies (Clark et al., 1990; Duke, 1994; Graham et al., 2018; Hunt, 1977; Kokaly et al., 2017b; Martínez-Alonso et al., 2002; Post and Noble, 1993; Swayze et al., 1992; Swayze et al., 2014) were consistent in demonstrating that the position of the white mica 2200 nm combination feature is highly dependent on the specific cations occupying the octahedral sites. This

relationship between Al^{oct} content and white mica 2200 nm combination feature position has been quantified in four spectral studies (Kokaly et al., 2017b; Lypaczewski et al., 2019; Post and Noble, 1993; Swayze et al., 2014). The relationship calculated in Swayze et al. (2014) indicates that a 1 nm shift in the white mica 2200 nm combination feature position corresponds to a change in Al^{oct} content of $\pm 1.06\%$ while Kokaly et al. (2017b) indicates that a 1 nm shift corresponds to a change in Al^{oct} content of $\pm 1.04\%$.

5.2. Base metal sulfide deposits

Deposits composed of massive zones of base metal sulfide minerals can form due to hydrothermal fluid circulation beneath the paleoseafloor in volcanic and amagmatic settings (David, 2018; Franklin et al., 2005; Guilbert and Park Jr, 2007; Simmons et al., 2005). Since mineralized zones commonly occur at the contact between the footwall and hanging wall, the transition in white mica alteration characteristics may be a useful exploration vector for high-grade ore zones (Shanks III et al., 2012).

Fig. 5 summarizes the results of spectral studies from twelve massive sulfide deposits. The smallest shift in the position of the white mica 2200 nm combination feature deemed significant in these studies was 1 nm (Huang et al., 2018; Laakso et al., 2016).

5.3. Epithermal deposits

Epithermal deposits are products of magmatic-hydrothermal activity and are important sources of gold, silver, and base metals. Epithermal deposits form in near-surface environments when hydrothermal fluids precipitate metals and alteration minerals in veins or disseminations (Cooke and Simmons, 2000; Hedenquist et al., 2000; Robb, 2004; Simmons et al., 2005). When fluid flow is concentrated in discrete fracture systems during vein formation, alteration characteristics will vary in the vein proper, at the vein margins, and in the unaltered host rocks. This variation will occur on a scale of meters to hundreds of meters. Fig. 6 summarizes spectral studies at four epithermal deposits. The smallest shift in the position of the white mica 2200 nm combination feature deemed significant in these studies was 2 nm (Yang et al., 1999).

5.4. Porphyry deposits

Porphyry deposits are large tonnage, low grade ore bodies which are the world's principal source of Cu and Mo (Seedorff et al., 2005; Sillitoe, 2010). The position of the white mica 2200 nm combination feature will typically trend shortwards towards the center of the hydrothermal system, where the highest temperature hydrothermal fluids traveled. Porphyry systems are associated with skarns and epithermal deposits, which will have differing spectral signatures than the host porphyry, leading to a complex geo-spectral deposit model. Fig. 7 shows the results of the wavelength position as it relates to mineralized zones. The smallest shift in the position of the white mica 2200 nm combination feature deemed significant in these studies was 1 nm (Graham et al., 2018; Kokaly et al., 2017b; Uribe-Mogollon and Maher, 2018, 2020).

5.5. Orogenic gold

Orogenic gold deposits are formed by the fault-focused ascent of hydrothermal fluids derived mainly from dehydration during regional metamorphism. These fluids are focused in major structural discontinuities, which can extend for kilometers along strike (Goldfarb et al., 2005). Zones of alteration several kilometers wide may occur from the vein margins into the host rock (Lypaczewski et al., 2019). The position of the white mica 2200 nm combination feature varied from 2194 to 2010 nm (Bierwirth et al., 2002) and the smallest shift deemed significant in the two reviewed studies was 1 nm (Lypaczewski et al., 2019).

5.6. Sedimentary rock hosted gold deposits

Sedimentary rock hosted gold deposits are disseminated hydrothermal replacement bodies hosted in sedimentary rocks in extensional settings in northern Nevada, USA (Cline et al., 2005). The spectral signature of sedimentary rock hosted gold deposits is spatially large, yet subtle. An ammoniated illite spectral signature may be used as a possible exploration vector (Mateer, 2010). The smallest shift in the position of the white mica 2200 nm combination feature deemed significant in the two reviewed studies was 1 nm (Ahmed et al., 2009; Mateer, 2010).

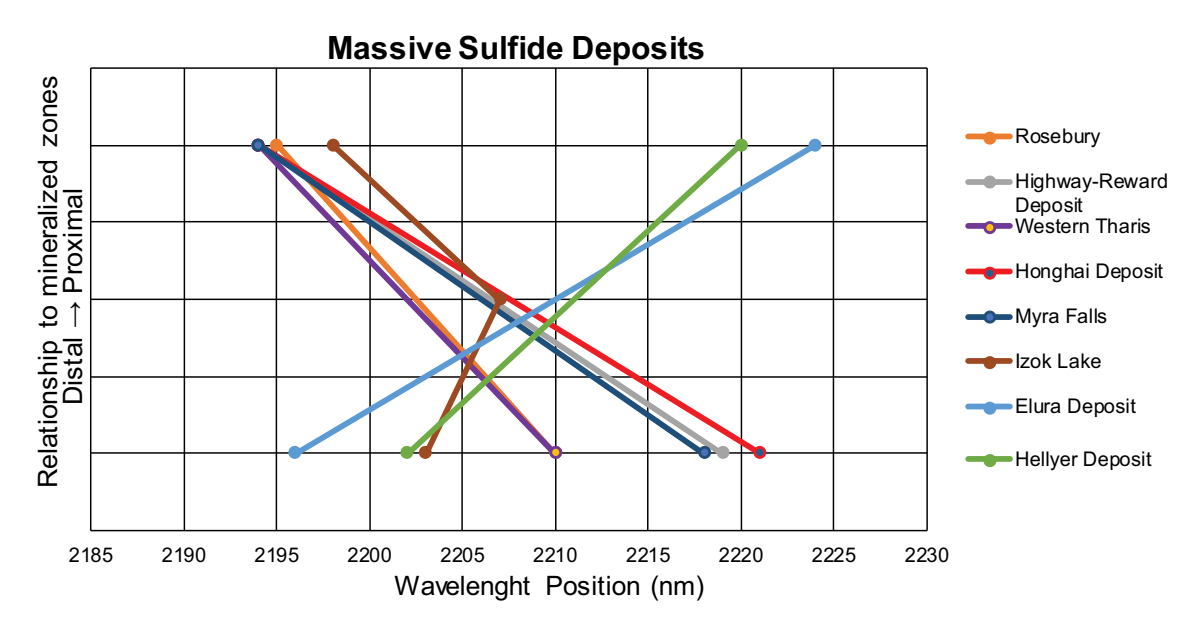


Fig. 5. Variation of white mica 2200 nm combination feature position with proximity to mineralized zones as reported for spectral studies conducted at massive sulfide deposits (Herrmann et al., 2001; Huang et al., 2018; Jones et al., 2005; Laakso et al., 2016; Lawrie and Hinman, 1998; Sun et al., 2001; Yang et al., 2011).

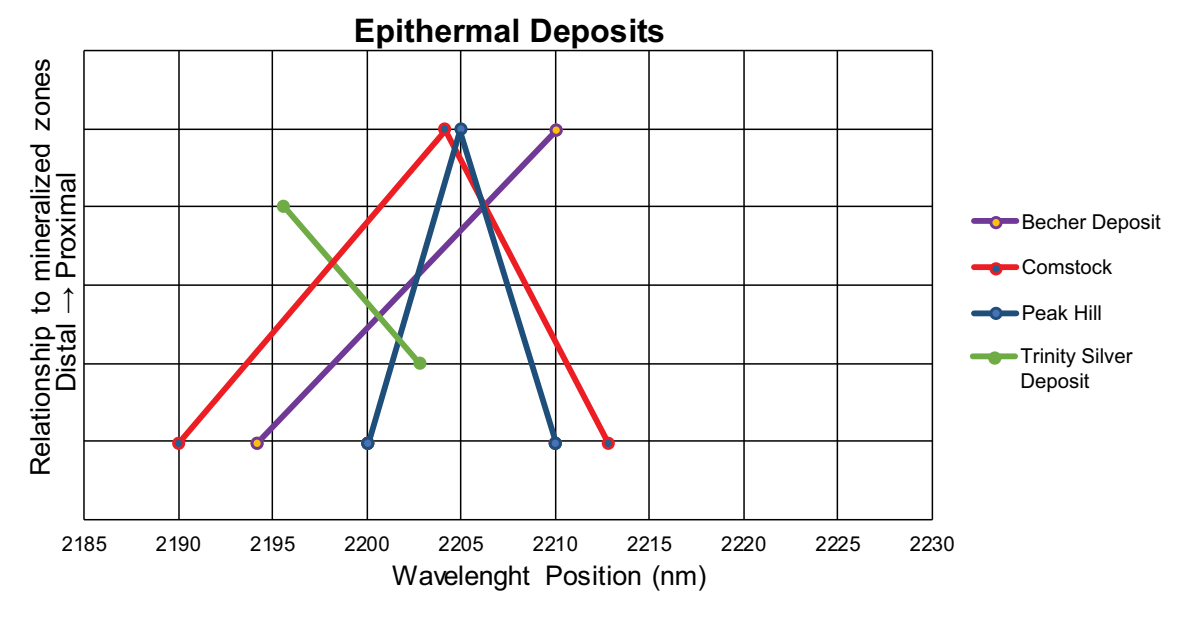


Fig. 6. Variation of white mica 2200 nm combination feature position with proximity to mineralized zones in epithermal deposits (Bierwirth et al., 2002; Huston et al., 2002; Kruse et al., 2012; Squire et al., 2007; Yang et al., 1999).

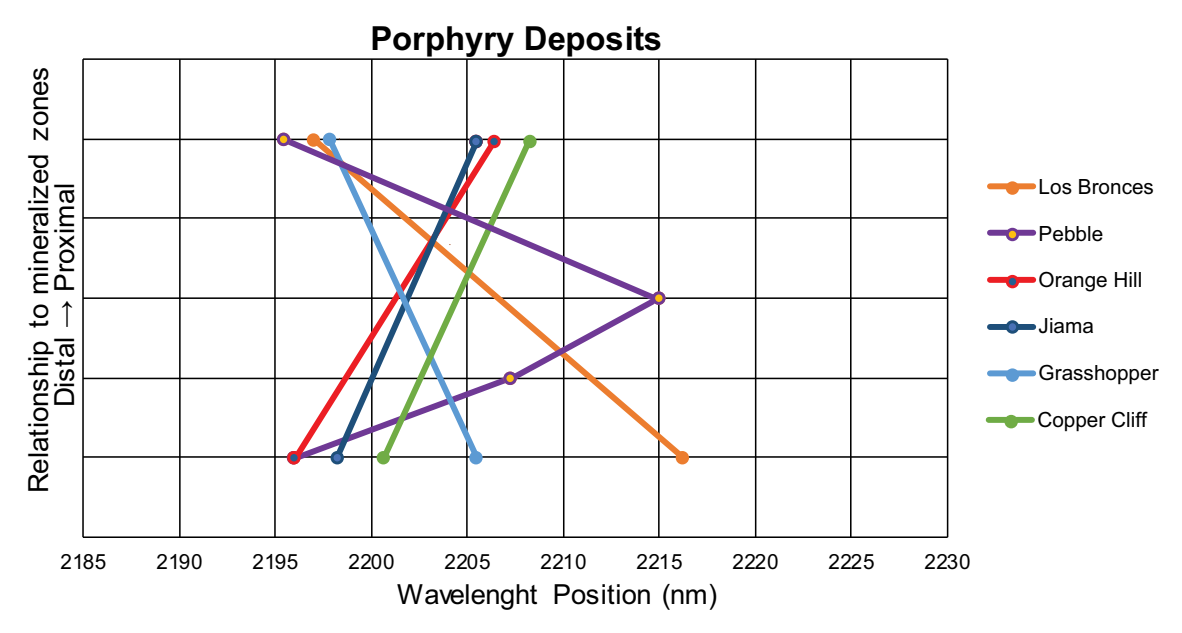


Fig. 7. Variation of white mica 2200 nm combination feature position with proximity to mineralized zones in porphyry systems (Agus, 2011; Dalm et al., 2017; Graham et al., 2018; Gregory et al., 2013; Guo et al., 2019; Harraden et al., 2013; Kokaly et al., 2017b; Lang et al., 2013; Uribe-Mogollon and Maher, 2018, 2020).

5.7. Iron oxide copper gold deposits

Iron oxide copper gold (IOCG) deposits are structurally controlled, large tonnage resources of Cu, Fe, and Au hosted in breccias (Hitzman et al., 1992). IOGC deposits differ from copper porphyry deposits mainly in their high concentration of iron oxides, typically hematite and magnetite (Hitzman et al., 1992). These deposits have large spatial footprints, with alteration halos extending for kilometers that may be investigated with remote sensing techniques (Groves et al., 2010; Hitzman et al., 1992; Robb, 2004). One spectral study conducted at an IOGC deposit and reviewed for this contribution determined that the position of the white mica 2200 nm combination feature varied from 2217 nm distal to mineralized zone to 2209 nm proximal to mineralized zones. The smallest shift in the position of the white mica 2200 nm combination feature deemed significant in this study was 4 nm (Tappert et al.,

2011).

5.8. Unconformity related uranium deposits

Unconformity related uranium deposits are formed where thick sequences of siliclastic sedimentary rocks lie unconformably above basement granites and metasedimentary rocks. Faults allow for the movement of metal-bearing solutions across the unconformity where changes in the redox environment cause precipitation of uranium (Jefferson et al., 2007). A distinct change in the spectral signature between the footwall and hanging wall, with alteration halos up to 6 km from the deposit, can be mapped (Mathieu et al., 2017). Illitization and chloritization of feldspars are the most common alteration types at Cigar Lake and these were readily mapped. Illites ranged from 2197 to 2210 nm, muscovite ranged from 2206 to 2210 nm, and phengite ranged from

2217 to 2222 nm. The smallest shift in the position of the white mica 2200 nm combination feature deemed significant in this study was 4 nm (Mathieu et al., 2017)

5.9. Discussion of white mica spectral studies

Laboratory studies indicate that the octahedral cation composition of white micas determines the position of the 2200 nm combination feature. Increased Al content (with a corresponding decrease in Fe and Mg as per the Tschermak substitutions) in the octahedral layer will shift the white mica 2200 nm combination feature shortwards. The smallest shift in the white mica 2200 nm combination feature that was deemed to be significant in the reviewed spectral studies was 1 nm. Thus, a spectrometer having a RMSE of 1 nm in the position of the white mica 2200 nm combination feature would be an appropriate instrument to use in studies like those reviewed.

6. Spectrometer sensitivity analysis

This section presents the results of a sensitivity analysis conducted to determine the effect of varying spectrometer characteristics on the ability to determine the wavelength position of the white mica 2200 nm combination feature. The goal of this analysis was to determine the characteristics that resulted in a root mean square error (RMSE) of 1 nm when determining the position of the white mica 2200 nm combination feature position. A spectrometer's design characteristics and performance (spectral range, sampling interval, bandpass, SNR, and spatial resolution) govern its ability to collect data suitable for identification and quantification of spectral features, including the white mica 2200 nm combination feature. This contribution focuses on the effects of bandpass, sampling interval, channel position, and SNR as they pertain to accurate characterization of the white mica 2200 nm combination feature. Spatial resolution will not be addressed in this contribution but should be considered when selecting an instrument for a particular study.

6.1. Background on spectrometer characteristics

The spectral response of a spectrometer is measured using four characteristics: spectral range, spectral sampling interval, spectral bandpass, and SNR (Clark, 1999; Kokaly et al., 2017b; Swayze et al., 2003). Imaging spectrometers are additionally characterized by the spatial resolution of each pixel (Goetz et al., 1985; Green et al., 1998). Spectral range is the region of the electromagnetic spectrum in which a spectrometer is sensitive. Sampling interval is the spectral distance between the centers of adjacent spectrometer channels. Spectral bandpass is defined as the Full Width Half Maximum (FWHM) response of a spectrometer channel to a monochromatic light and describes the wavelength interval over which each channel of a spectrometer is sensitive (Kokaly et al., 2017a; Swayze et al., 2003). Channel position is the center of the spectral bandwidth of a channel (Clark, 1999). Signal to noise ratio is equal to the mean signal level divided by one standard deviation of the signal fluctuations (Swayze et al., 2003). Spatial resolution is relevant to imaging spectrometers only, an analogous characteristic in point spectrometers is field of view (FOV). Spatial resolution is defined as the smallest object that can be resolved in an image and is commonly reported as the linear dimension on the ground of an individual pixel in a remotely sensed image (Liang et al., 2019). Spectral resolution is controlled by sampling interval and bandpass and is defined as twice the bandpass in spectrometers that critically sample spectra (Swayze et al., 2003). Fine spectral resolution spectrometers have small sampling intervals and bandpasses while coarse spectral resolution spectrometers have large sampling intervals and bandpasses.

The quality of data acquired by a spectrometer is dependent upon the above characteristics and their interrelatedness. Bandpass and sampling interval combine to determine a spectrometer's spectral sampling (Swayze et al., 2003). Decreasing the sampling interval will partition the data into finer regions but decreases the SNR as fewer photons are falling on each detector, while noise, especially intrinsic instrument noise, remains at the same level. Thus, sampling interval and SNR are dependent characteristics of a spectrometer's performance. Bandpass is dependent upon detector size, detector performance, and the instruments optical geometry. Bandpass is independent of sampling interval, and thus independent of SNR (Swayze et al., 2003). Bandpass and sampling interval are the preferred parameters to use when reporting spectrometer characteristics.

Swayze et al. (2003) discuss the difficulty in simultaneously modeling sampling interval, bandpass, and SNR due to the interdependence of these parameters. Swayze et al. (2003) determined that identification accuracy is strongly influenced by the SNR at small sampling intervals but is controlled by sampling interval itself at large sampling intervals due to spectral biasing. The present contribution initially used noiseless data for all the modeled spectrometers when determining the ideal sampling interval, bandpass, and channel position required to characterize the 2200 nm white mica combination feature. Once these characteristics are determined, noise is introduced to the reflectance data to measure its effect on the RMSE of the position determination.

6.2. Selection of software for the sensitivity analysis

A wide variety of software and methods were used to determine the position of the white mica 2200 nm combination feature in the reviewed studies. Considering the ability for expert user input to the process, in addition to the increased performance of estimating a features position using a quadratic function fitted to three channels, it was determined that the U.S. Geological Survey (USGS) PRISM software suite (Kokaly, 2011) was an appropriate selection for the spectral analysis conducted for this contribution.

Analytical tools within PRISM were used to perform mathematical operations on spectra such as convolving data, performing continuum removal on absorption features, and generating statistics on those features (Kokaly, 2011). Spectral features, such as the white mica 2200 nm combination feature, are identified and analyzed in PRISM with user selected fixed continuum endpoints and PRISM adjusted continuum endpoints. The position of an absorption feature is determined by measuring a fitted quadratic function to the feature's band center and the channel on either side, similar to the minimum wavelength mapper (Bakker et al., 2011; Clark et al., 2003; Duke, 1994; van Ruitenbeek et al., 2014).

6.3. Sensitivity analysis methods

Sensitivity analyses were performed using the following general procedures;

- Selection of spectra of high quality white mica mineral samples from the USGS spectral library (Kokaly et al., 2017a) to be used as reference spectra,
- Convolution of the reference spectra to a variety of actual and theoretical spectrometer characteristics,
- Determination of the white mica 2200 nm combination feature position of the reference and convolved spectra using spectral feature analysis.
- Comparison and analysis of the white mica wavelength position of the reference spectra and the convolved spectra,
- 5. Determination of best performing spectrometer characteristics,
- 6. Analysis of the effects of varying the SNR of the convolved reference spectra on the determination of the RMSE of the white mica 2200 nm combination feature position using three selected spectrometers.

6.3.1. Sample selection and convolution of spectra

The USGS Spectroscopy Laboratory in Lakewood, Colorado maintains a library of minerals and mineral spectra that are used as standards for spectral studies (Kokaly et al., 2017a). Nineteen white mica samples from various field sites were used in this analysis and are listed in the supplemental materials. All samples are classified as pure based on significant supporting data. Spectra were obtained using the USGS Spectroscopy Laboratory's Nicolettm Fourier Transform Infrared (FTIR) spectrometers (see Table 1 for spectrometer details) in a controlled laboratory setting. The Nicolet FTIR spectrometers have a combination of a narrow sampling interval of 1 nm, narrow bandpass of 1.94 at 2200 nm, high SNR, and highly accurate reported wavelength position that generate high resolution spectra precise enough to be considered as reference spectra for this study. The position of the white mica 2200 nm combination feature of the 19 samples varied from 2183.8 to 2223.0 nm with an average position of 2205.0 nm. The USGS PRISM software was used to convolve Nicolet reference spectra having fine spectral resolution to coarse spectral resolution (coarse sampling and bandpass) characteristics, simulating the measurement of these samples by 29 spectrometers. Of the 29 spectrometers, five were point spectrometers of existing design, 12 were imaging spectrometers of existing design, and 12 had theoretical sampling interval and bandpass characteristics (Table 1). This convolution method followed a well-established approach wherein spectra generated from the convolution of fine spectral data to coarse spectral data are used to test the specifications of a proposed spectrometer (Clark, 1993; Hewson et al., 2005; Kokaly, 2011; Kokaly et al., 2017a; Kokaly et al., 2017b; Swayze et al., 2003; Yang et al., 1999). By convolving fine spectra of known minerals to the modeled characteristics of a variety of spectrometers, it is possible to isolate the effect of varying the bandpass and sampling interval on the accurate determination of spectral features. This approach is feasible because it removes the effects of inherent variations in natural samples that otherwise would be propagated through the data if samples were measured at differing times with multiple instruments of varying characteristics. The native Nicolet reference spectra have very high SNR and convolution of these reference spectra will increase this native SNR. For these reasons, the convolved Nicolet spectra used in this study can be considered essentially noiseless.

The reference spectra and the convolved spectra were analyzed using the 'white mica 2200 nm mineral feature analysis' routine contained within the PRISM framework (Kokaly, 2011). The routine generates a variety of parameters, including the position of the 2200 nm combination feature for each tested spectrum, and outputs these as a text file. The measured white mica 2200 nm combination feature position parameters of the 19 convolved spectra were compared to those of the respective 19 reference spectra. Regression analysis was performed to generate regression equations and R² fit values for the white mica 2200 nm combination feature position as measured by the Test Spectrometers compared to the reference spectra. The RMSE was calculated for the white mica 2200 nm combination feature position determination for each spectrometer as compared to the position as determined with the reference Nicolet spectra (Table 1). Because the RMSE is calculated from convolved reference spectra that are essentially noiseless, this value indicates the error associated with varying sampling interval and bandpass, with no error contributed by noise. The effect of noise on RMSE is calculated in Section 6.3.3.

6.3.2. Channel-shifted spectrometers

A sensitivity analysis was conducted to determine the effect of shifting the spectrometer channel centers in increments of 1 nm on the determination of the white mica 2200 nm combination feature wavelength position. Ten 'Channel-Shifted Spectrometers' were created with a sampling interval and bandpass of 10 nm, characteristics that were chosen as these are the likely spectrometer characteristics that may be deployed on near future orbital platforms such as the Earth Surface Mineral Dust Source Investigation (EMIT), the Surface Biology and

Table 1

Characteristics of the Nicolettm spectrometers used to measure reference spectra and the 29 'Test Spectrometers' used to conduct the white mica 2200 nm wavelength position sensitivity analysis. The reported sampling interval and the bandpass of each spectrometer near the 2200 band is given. The RMSE is given for the position of the white mica 2200 nm combination feature in the 19 white mica Nicolet reference spectra convolved to the characteristics of each Test Spectrometer as compared to the native Nicolet reference spectra.

Reference Spectrometers	Sampling Interval at 2200 nm	Bandpass at 2200 nm	RMSE Position (nm)
Nicolet Fourier Transform Infra- red (Nicolet) - model 740 (prior to 1998), model Magna 760 (1998–2008), model 6700 (2008 to present) ^a	1 (model 6700)	1.94 (model 6700)	n/a
Test Spectrometers	Sampling Interval at 2200 nm	Bandpass at 2200 nm	RMSE Position (nm)
Point Spectrometers ASD Full Range Standard Resolution (ASDFR) ^b	1.0	11.2	0.97
ASD FS3 High-Resolution (ASDHR) ^c	1.0	8.9	0.88
ASD FS4 Next Generation (ASDNG) ^d	1.0	5.6	0.72
Beckman tm 5270 (Beckman) ^e	10.0	10.0	1.15
Spectral Evolution ^f	1.0	3.0	0.28
Imaging Spectrometers			
AVIRIS 1989 ^g	10.0	11.1	1.09
AVIRIS 1996 (AVIRIS-classic) ^h	10.0	9.6	1.17
AVIRIS NG ^h	5.0	5.9	0.83
Corescan® HCI-III ⁱ	4.0	11.3	1.01
HyMap 1999 ^j	18.0	19.3	2.03
НуМар 2007 ^ј	19.1	21.4	2.21
HyMap2 2014 ^j	17.2	18.2	2.13
Hyperion 221ch ^k	10.1	10.6	1.22
HySpex tm SWIR 384 ¹	5.5	7.0	0.95
SpecTIR® AisaFENIX 1K (FX1) Cuprite ^m	6.2	7.7	0.99
SpecTIR® AisaFENIX 1K (FX1) 2017 ^m	6.2	7.7	0.94
SpecTIR® AisaFENIX 1K (FX2) 2018 ^m	6.1	8.1	0.96
Theoretical Spectrometers			
Theoretical 01_01	1.00	1.00	0.26
Theoretical 01_05	1.00	5.00	0.65
Theoretical 01_10	1.00	10.00	0.93
Theoretical 02	2.00	2.00	0.22
Theoretical 05	5.00	5.00	0.80
Theoretical 10	10.0	10.0	1.20
Theoretical 15	15.0	15.0	1.57
Theoretical 20	20.0	20.0	2.35
Theoretical 25	25.0	25.0	2.77
Theoretical 30	30.0	30.0	4.51
Theoretical 35	35.0	35.0	4.31
Theoretical 40	40.0	40.0	6.71

^a Nicolet Instrument Corporation (1997) Magna-IR FTIR Spectrometers System 560 and 760 User's Guide 2020 http://nano.ee.uh.edu/Text/Nicolet%20Magna-IR%20560%20Manual.pdf, ThermoFisher Scientific (2019) Nicolet FTIR Instruments November 29, 2019 https://www.thermofisher.com/us/en/home/industrial/spectroscopy-elemental-isotope-analysis/molecular-spectroscopy/fourier-transform-infrared-ftir-spectroscopy/ftir-instruments.html

b Malvern Panalytical (2018b) ASD FieldSpec®range December 10, 2018 http s://www.malvernpanalytical.com/en/products/product-range/asd-range/fi eldspec-range/index.html

c Ibid.

d Malvern Panalytical (2018a) ASD FieldSpec® 4 Hi-Res NG Spectroradiometer https://www.malvernpanalytical.com/en/products/product-range/asd-range/fieldspec-range/fieldspec-4-hi-res-ng-spectroradiometer/

^e Clark et al. (1990). High spectral resolution reflectance spectroscopy of minerals. *Journal of Geophysical Research: Solid Earth*, 95 (B8) 12653–12,680 https://doi.org/10.1029/JB095iB08p12653.

f Spectral Evolution Inc (2019) Products 2019 https://spectralevolution.com/products/

- ⁸ Green et al. (1998). Imaging spectroscopy and the airborne visible/infrared imaging spectrometer (AVIRIS). *Remote Sensing of Environment,* 65 (3) 227–248 https://doi.org/10.1016/S0034-4257(98)00064-9.
- h Hamlin et al. (2011). Imaging spectrometer science measurements for terrestrial ecology: AVIRIS and new developments. In, 2011 Aerospace Conference 1–7. Blg Sky, Montana, USA: IEEE https://doi.org/10.1109/AERO.2011. 5747395.
- i Corescan Pty Ltd (2019) The Corescan System 2019 http://www.corescan.com.au/services/the-corescan-system
- ^j Cocks et al. (1998). The HyMapTM airborne hyperspectral sensor: the system, calibration and performance. In, *Proceedings of the 1st EARSeL Workshop on Imaging Spectroscopy* 37–42. Zurich, Switzerland: EARSeL
- ^k Pearlman et al. (2003). Hyperion, a space-based imaging spectrometer. *IEEE Transactions on Geoscience and Remote Sensing*, 41 (6) 1160–1173 https://doi.org/10.1109/TGRS.2003.815018.
- Norsk Elektro Optikk AS (2016) HySpex SWIR-384 June 2, 2017 http://www.hyspex.no/products/
- ^m SpecTIR Inc (2018) Featured Instruments 2019 https://www.spectir.com/technology#featured-instruments

Geology (SBG) observing system, and the Environmental Mapping and Analysis Program (EnMAP) hyperspectral imaging spectrometer (Green et al., 2018; Kokaly and Turpie, 2019; Sang et al., 2008). Each successive spectrometer was created with the channel centers shifted 1 nm towards longer wavelengths, thus shifting the channel centers near the 2200 nm position in 1 nm increments. See supplemental materials for details of these spectrometers. Because the sampling interval of this set of spectrometers was 10 nm, the position of channel centers adjacent to the 2200 nm combination feature is repeated every ten iterations. The procedure for testing these 10 channel-shifted theoretical spectrometers was similar as described for the 29 Test Spectrometers above. The 19 reference spectra were convolved to the characteristics of the 10 Channel-Shifted Spectrometers, the white mica mineral feature analysis was performed, and the reported white mica 2200 nm combination feature position was compared to the reported position of the reference spectra. The RMSE was calculated for the position determination of the white mica 2200 nm combination feature for each spectrometer.

6.3.3. Signal to noise analysis

After determining the spectrometer characteristics required to achieve a RMSE of 1 nm of the white mica 2200 nm combination feature position of the noiseless convolved Nicolet spectra compared to the reference Nicolet spectra, a noise component was introduced to analyze the effect of lowering the SNR on the RMSE of the position measurement. In this study, noise was simply added to the reflectance data; however, a more complete treatment of imaging spectrometer design should consider noise in the radiance data and the introduction of systematic errors in computed reflectance (Thompson et al., 2019). Three spectrometers were selected for this SNR analysis, Theoretical 01 01, Theoretical 05, and Theoretical 8.9 9.9. Theoretical 01 01 and Theoretical 05 were determined to have RMSE's of 0.26 and 0.8 nm respectively in the position measurement when comparing convolved spectra of the 19 white mica samples to the reference Nicolet spectra. Analysis of these spectrometers will determine the minimum SNR required to achieve a RMSE of 1, 1.5, and 2 nm when measuring the position of the white mica 2200 nm combination feature with spectrometers having these characteristics. An additional theoretical spectrometer, Theoretical 8.9_9.9, was created with a sampling interval of 8.9 nm and a bandpass of 9.9 nm. These were the coarsest characteristics that were determined to give a RMSE of 1 nm in the measurement of the white mica 2200 nm combination feature position of convolved spectra (see Section 6.4.4). Analysis of this spectrometer will provide guidance as to the expected RMSE as signal is degraded with increasing noise. Measurements of the position of the 2200 nm white mica combination feature of the noisy spectra will be compared to the position of the feature in the respective convolved spectra, not the reference Nicolet spectra, to isolate the effects of adding the various noise levels to the data.

The first step in the SNR analysis was a determination of the number of noisy spectra required to be simulated to perform a robust determination of the RMSE in the measurement of the white mica 2200 nm combination feature position. Nicolet reference spectra of two white mica samples were convolved to the characteristics of the three SNR test spectrometers. Gaussian noise was added to create 10,000 noisy spectra with SNR's of 25, 50, 100, 250, 500, and 1000 for each of the three test spectrometers. The RMSE of the position of the 2200 nm white mica combination feature of the noisy spectra as compared to the position of the feature in the noiseless convolved Nicolet reference spectra was determined for sample sizes ranging from 25 to 10,000 for each spectrometer. These results were then examined to determine the number of noisy spectra that must be tested to achieve a stable RMSE value at various SNR for each of the three SNR analysis spectrometers (Table 2). To simplify the testing process, the largest sample size required (n=7500) was then used for all three spectrometers at all SNR levels (see Section 6.4.4).

Gaussian noise at SNR's of 25, 50, 100, 250, 500, and 1000 was added to Nicolet reference spectra of the 19 white mica reference samples convolved to the characteristics of the three SNR test spectrometers. A reflectance level of 50% was assumed for the noise calculation. The RMSE of the position of the 2200 nm white mica combination feature of the 7500 noisy spectra as compared to the position of the feature in the noiseless convolved spectra was then determined for each spectrometer. Measurements were made with user-selected fixed and automatically adjusted continuum endpoints. Sample GDS87 was not used in the SNR analysis as it required the hand-picking of the right continuum endpoint. This was deemed too labor intensive to perform on the 7500 noisy spectra generated for the SNR analysis. The elimination of this one sample, leaving 18 white mica samples, is assumed to not significantly affect the results.

Lastly, the SNR required to achieve cumulative RMSE's of 1, 1.5, and 2 nm was calculated for the three SNR analysis spectrometers. Cumulative RMSE is defined as the RMSE that is introduced by varying the sampling interval and bandpass characteristics, determined in the sensitivity analysis using noiseless convolved white mica spectra, plus the RMSE determined in the SNR analysis using the convolved white mica spectra with added noise.

6.4. Sensitivity analysis results

The impacts on the RMSE of the position of the 2200 nm white mica combination feature position of varying bandpass, sampling interval, channel centers, and SNR are presented. Recalling that most spectral studies reviewed in this contribution identified a shift of 1 to 2 nm in the position of the white mica 2200 nm as being significant, the bandpass, sampling interval, and SNR required to achieve a RMSE of 1 nm and 2 nm are discussed in the following sections.

6.4.1. Impact of varying sampling interval on position measurement

The initial sensitivity analysis was conducted using the noiseless Nicolet reference spectra convolved to the characteristics of the 29 test spectrometers. The RMSEs of the position of the white mica 2200 nm

Table 2
Minimum number of noisy spectra samples required to produce robust measurements of the position of the white mica 2200 nm combination feature.

SNR	Theoretical 01_01 Sample Size	Theoretical 05 Sample Size	Theoretical 8.9_9.9 Sample Size
25	7500	7500	5000
50	7500	7500	4000
100	7500	5000	4000
250	5000	5000	4000
500	5000	4000	4000
1000	2500	2500	2000

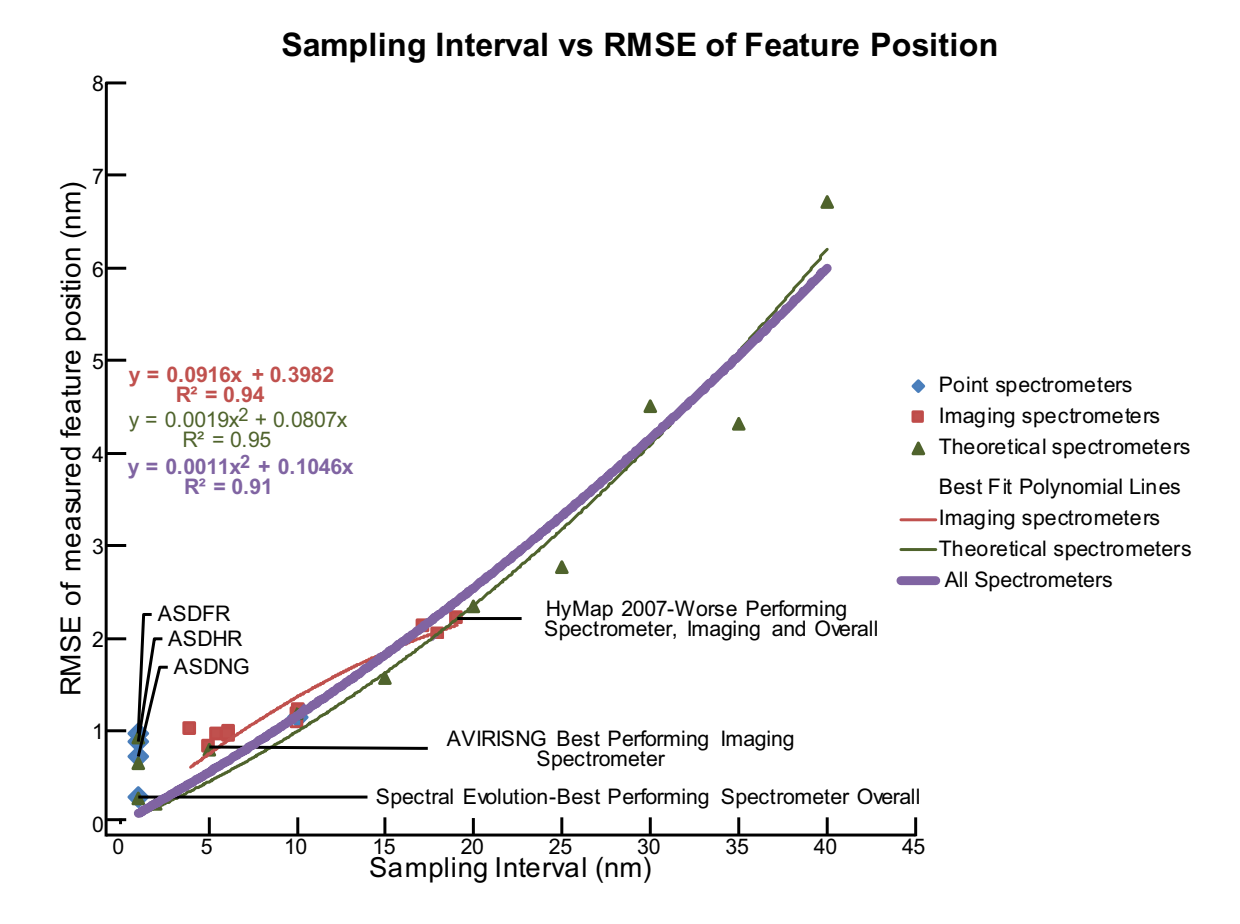


Fig. 8. Root Mean Square Error (RMSE) the white mica 2200 nm combination feature position of 19 USGS white mica samples as determined for five point spectrometers, twelve imaging spectrometers, and twelve theoretical spectrometers with various sampling intervals. Fit lines for the imaging, theoretical, and all spectrometers are given. A RMSE of 1 nm was achieved at a sampling interval of 8.8 nm.

combination feature as the sampling interval varied are shown in (Fig. 8) and ranged from 0.28 nm (Spectral Evolution) to 6.71 nm (Theoretical 40). A RMSE of 1 nm in determining the position of the white mica 2200 nm combination feature is achievable with a spectrometer having a sampling interval of 8.8 nm. A RMSE of 2 nm in determining the position of the white mica 2200 nm combination feature is achievable with a spectrometer having a sampling interval of 16.3 nm.

Little to no variation is shown in the RMSE of the white mica 2200 nm combination feature position as determined with spectrometers having similar bandpasses but differing sampling intervals. For example, five spectrometers have a bandpass of 10 nm, +/- 0.57 nm, the Beckman 5270 (SI-10, BP-10), the AVIRIS 1996 (SI-10, BP-9.6), the Hyperion 221ch (SI-10.10, BP-10.57), Theoretical 01_10 (SI-1, BP-10), and Theoretical 10 (SI-10, BP-10). The RMSE of the white mica 2200 nm combination feature position varied from 0.93 (Theoretical 01_10) to 1.22 (Beckman 5270) nm in these five spectrometers. The best imagining spectrometer was the AVIRIS NG (SI-5.0, BP-5.86) with a RMSE of 0.83 nm, while the worse performing imaging spectrometer, and worse performing spectrometer overall, was the HyMap 2007 (SI-19.1, BP-21.40) with a RMSE of 2.21. No clustering or segregation by instrument type (theoretical, point, or imaging) was observed in the reported RMSE. The following equation can be used to determine the sampling interval required to achieve a specified RMSE for the determination of the white mica 2200 nm combination feature:

RMSE (nm) = $0.0011 \times {}^{2} + 0.1046 \times {}$

where x = Sampling interval (nm).

6.4.2. Impact of varying bandpass on position measurement

The RMSE of the position of the white mica 2200 nm combination feature in noiseless data as the bandpass is varied in each of the 29 Test Spectrometers is shown in Fig. 9. A RMSE of 1 nm in determining the position of the white mica 2200 nm combination feature is achievable with a spectrometer having a bandpass of 9.8 nm. A RMSE of 2 nm in determining the position of the white mica 2200 nm combination feature is achievable with a spectrometer having a bandpass of 17.5 nm.

As sampling interval is held constant, RMSE of the white mica 2200 nm combination feature position decreases with finer bandpass. Four of the five point spectrometers have sampling intervals of 1 nm. The ASDFR (SI-1, BP-11.2), ASDHR (SI-1, BP-8.9), ASDNG (SI-1, BP-5.6), and the Spectral Evolution (SI-1, BP-3), give progressively lower RMSE of the white mica 2200 nm combination feature position as bandpass is decreased, with a RMSE of 0.97 nm, 0.88 nm, 0.72 nm, and 0.28 nm respectively. A similar effect is seen in the Theoretical spectrometers. As bandpass is decreased from 10 nm in Theoretical 01_10, to 5 nm in Theoretical 01_05, and finally to 1 nm in Theoretical 01_01, RMSE decreases from 0.93 nm to 0.65 nm, and finally to 0.26 nm respectively. The five spectrometers (one point, three imaging, and one theoretical) with a sampling interval near 10 nm also show shifts in the RMSE as bandpass is varied, although the effect is not nearly as pronounced as the effect at a sampling interval of 1 nm, decreasing from 1.22 to 1.09 nm. The overlapping calculated ranges of RMSE's of the four point and three theoretical spectrometers having a sampling interval of 1 nm validates the use of theoretical spectrometers to model current and future spectrometers. No excessive variation between theoretical and actual spectrometers having similar characteristics was observed. The following equation can be used to determine the bandpass

Bandpass vs RMSE of Feature Position RMSE of measured feature position (nm) $=-0.0125x^2 + 0.2666x - 0.4027$ $R^2 = 0.93$ Point spectrometers $= 0.0026x^2 + 0.0247x + 0.6062$ $R^2 = 0.96$ Imaging spectrometers $0.0019x^2 + 0.0782x$ Theoretical spectrometers $R^2 = 0.97$ $0.0017x^2 + 0.0849x$ Best Fit Polynomial Lines $R^2 = 0.96$ HyMap 2007 Worse Imaging spectrometers Performing, Imaging Spectrometer and Overall Theoretical spectrometers VIRIS 1996 All Spectrometers AVIRIS NG-Best Performing Imaging Spectrometer Hyperion 221 Beckman 5270 Spectral Evolution Best

Fig. 9. Root Mean Square Error (RMSE) the white mica 2200 nm combination feature position of 19 USGS white mica samples as determined for five point spectrometers, twelve imaging spectrometers, and twelve theoretical spectrometers with various bandpasses. Fit lines for the point, imaging, theoretical, and all spectrometers are given. A RMSE of 1 nm was achieved at a bandpass of 9.8 nm.

Performing Overall

Bandpass (nm)

required to achieve a specified RMSE for the determination of the white mica 2200 nm combination feature:

RMSE (nm) =
$$0.0017 \times {}^2 + 0.0849 \times {}$$

where x = Bandpass (nm).

6.4.3. Impact of varying channel center on position measurement

The RMSE for the determination of the position of the white mica 2200 nm combination feature as the channel center is shifted in each of the ten Channel-Shifted Spectrometers varied from 1.06 to 1.25 nm, with an average RMSE of 1.16 nm. The range of variation of white mica 2200 nm combination feature position determination relative to the mean RMSE for all channel-shifted spectrometers was 15.7%. Channel-Shifted Spectrometer 5, with a channel centered on 2205 nm, the average of the 19 mineral samples, had a RMSE of 1.147 nm, essentially mid-way between the worst and best performing spectrometers.

6.4.4. Sample size selection for SNR analysis

The minimum number of noisy spectra that need to be simulated are given in Table 2. As the SNR was decreased, the standard deviation and the RMSE of the position measurement increased, necessitating the use of a larger sample size of noisy spectra to achieve a stable RMSE. Finer spectrometers, such as the Theoretical 01_01, require the simulation of more noisy spectra than coarser spectrometers to produce a robust estimation of RMSE.

6.4.5. Impact of SNR on RMSE of position measurement

The impact of SNR on the RMSE of the position of the white mica 2200 nm combination feature of 7500 noisy spectra compared to the

convolved Nicolet reference spectra is given for the three test spectrometers. The RMSE of the noiseless convolved Nicolet spectra, the RMSE contributed by the noisy test spectra, and the cumulative RMSE is given for the three SNR test spectrometers (Table 3).

Measurements taken with the Theoretical 01_01 spectrometer (Fig. 10) had lower RMSE's at given SNR levels than measurements taken with the Theoretical 05 (Fig. 11) and the Theoretical 8.9_9.9 (Fig. 12). Increasing the SNR in all spectrometers resulted in progressively smaller improvements in the RMSE of the measurement of the feature position. Using adjusted continuum endpoints produced lower RMSE's than using fixed continuum endpoints, particularly at low SNR levels.

Table 4 lists the minimum SNR required to achieve a specific cumulative RMSE in the measurement of the position of the 2200 nm white mica combination feature in noisy data.

6.5. Discussion of spectrometer sensitivity analyses

Spectral studies have been proven valuable in the characterization of mineral occurrences, specifically white micas, at the outcrop, deposit, and regional scale. From a practical point of view, it will be beneficial to determine the spectrometer characteristics and SNR that would be required to collect spectral data that will be appropriate for these types of studies.

The spectrometers with narrow sampling interval performed best in this study. Increasing bandpass, while holding the sampling interval constant, decreased the accuracy of determining the white mica 2200 nm combination feature position of noiseless convolved spectra in spectrometers with a narrow sampling interval. Varying sampling

Table 3Cumulative RMSE determined for the three SNR test spectrometers. Cumulative RMSE is defined as the RMSE of the noiseless convolved Nicolet reference spectra and the RMSE contributed by the noisy spectra.

	SNR - 25	SNR - 50	SNR - 100	SNR - 250	SNR - 500	SNR - 1000
Theoretical 01_01						
Spectrometer						
RMSE of convolved noiseless Nicolet spectra (nm)	0.26	0.26	0.26	0.26	0.26	0.26
Noise component	1.89	1.24	1.01	0.75	0.57	0.40
RMSE (nm)						
Cumulative RMSE	2.15	1.50	1.27	1.01	0.83	0.66
(nm)						
Theoretical 05						
Spectrometer						
RMSE of convolved	0.8	0.8	0.8	0.8	0.8	0.8
noiseless Nicolet spectra (nm)						
Noise component	1.48	0.81	0.51	0.30	0.16	0.07
RMSE (nm)						
Cumulative RMSE	2.28	1.61	1.31	1.10	0.96	0.87
(nm)						
Theoretical 8.9_9.8						
Spectrometer						
RMSE of convolved	1.0	1.0	1.0	1.0	1.0	1.0
noiseless Nicolet						
spectra (nm)						
Noise component	1.56	0.75	0.33	0.13	0.09	0.03
RMSE (nm)						
Cumulative RMSE	2.56	1.75	1.33	1.13	1.09	1.03
(nm)						

interval while holding bandpass constant had less of an effect on the RMSE of the position determination than did varying bandpass while holding sampling interval constant. A clear trend in increasing bandpass and decreasing accuracy in determining position was evident. Therefore, while Swayze et al. (2003) determined that bandpass was less critical to spectral mineral identification than SNR in spectrometers with small

sampling intervals, the results presented here expand upon those findings, indicating that when SNR is held constant, and sampling interval is approximately 10 nm, bandpass plays a more important role in the accuracy of a spectrometer than does sampling interval. As expected, increasing noise, and thus decreasing the SNR, resulted in larger RMSE when measuring the white mica 2200 nm combination feature position.

When tested assuming a high SNR, some imaging spectrometers performed well in this study, indicating their potential usefulness in field studies leveraging the white mica 2200 nm combination feature position. The AVIRIS 1996 (AVIRIS-Classic), AVIRIS NG, HySpex 384, AisaFENIX 1K (FX1), AisaFENIX 1K (FX2), and Corescan HCI-III all had a RMSE near 1 nm when determining the position of the white mica feature in noiseless data. The HyMap 1999, a spectrometer widely used in spectral studies, has a calculated RMSE of the position determination of 2.03 nm. The AVIRIS NG imaging spectrometer (SI-10.0, BP-9.6) with a RMSE of 0.83 nm, is comparable in accuracy to the ASDHR point spectrometer (SI-1.0, BP-8.9) which has a RMSE of 0.88 nm when determining position of the white mica 2200 nm combination feature. The AisaFENIX 1K (FX2) imaging spectrometer (SI-6.1, BP-8.1) with a RMSE of 0.96 nm is comparable in accuracy to the ASDFR point spectrometer (SI-1, BP-11.2) which has a RMSE of 0.97 nm when determining the position of the white mica 2200 nm combination feature.

The position of the center of the channels had some effect on the spectrometers ability to accurately determine the position of the white mica feature, however this degradation in performance was not significant and would not seem to be a design consideration for a general-purpose instrument deployed in a field setting.

The number of spectra required to produce a robust RMSE calculation when measuring the white mica 2200 nm combination feature varied based on the spectrometer used and the SNR of the measured spectra. As SNR of the collected spectra decreases for a particular spectrometer, the number of spectra that must be collected increases. Fine spectrometers, for example 1 nm sampling interval and bandpasss, require the collection of more spectra to produce robust test results at a given SNR than coarser spectrometers. When measuring the same absorption feature, fine spectrometers will record smaller absolute variation in signal strength in adjacent channels than coarser spectrometers due to their smaller sampling interval. For example, when measuring the

Theoretical 01_01

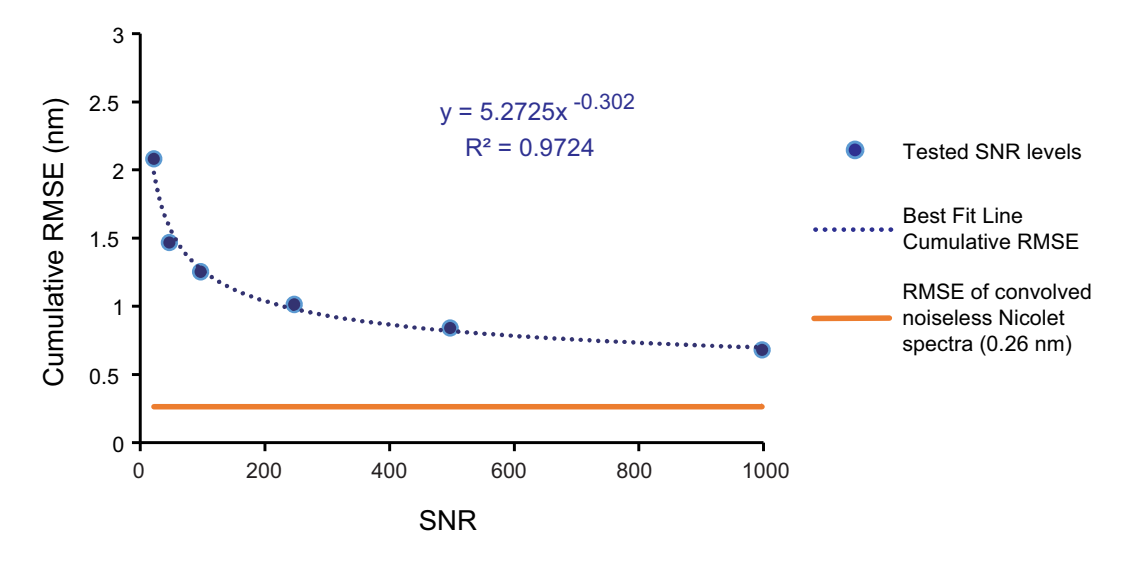


Fig. 10. Gaussian noise was added at SNR's of 25, 50, 100, 250, 500, and 1000 to 7500 Nicolet spectra convolved to the characteristics of the Theoretical 01_01 spectrometer. The position of the white mica 2200 nm combination feature in the noisy spectra was compared to the position in the convolved noiseless Nicolet spectra and the RMSE was determined for each SNR. The cumulative RMSE is the sum of the RMSE of the convolved noiseless Nicolet spectra, and the RMSE that results from the addition of noise.

Theoretical 05

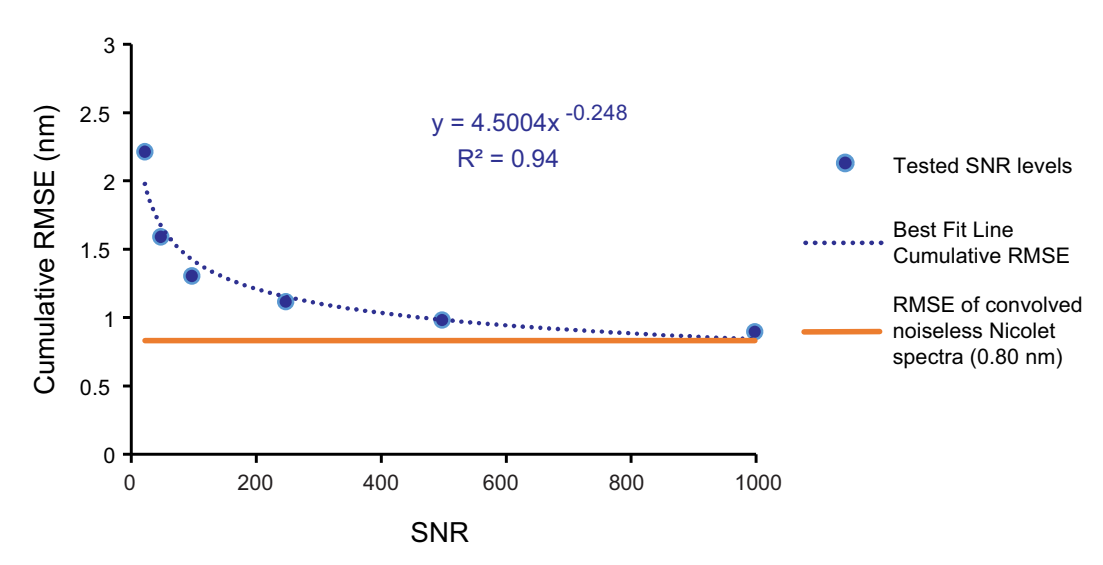


Fig. 11. Gaussian noise was added at SNR's of 25, 50, 100, 250, 500, and 1000 to 7500 Nicolet spectra convolved to the characteristics of the Theoretical 05 spectrometer. The position of the white mica 2200 nm combination feature in the noisy spectra was compared to the position in the convolved noiseless Nicolet spectra and the RMSE was determined for each SNR. The cumulative RMSE is the sum of the RMSE of the convolved noiseless Nicolet spectra, and the RMSE that results from the addition of noise.

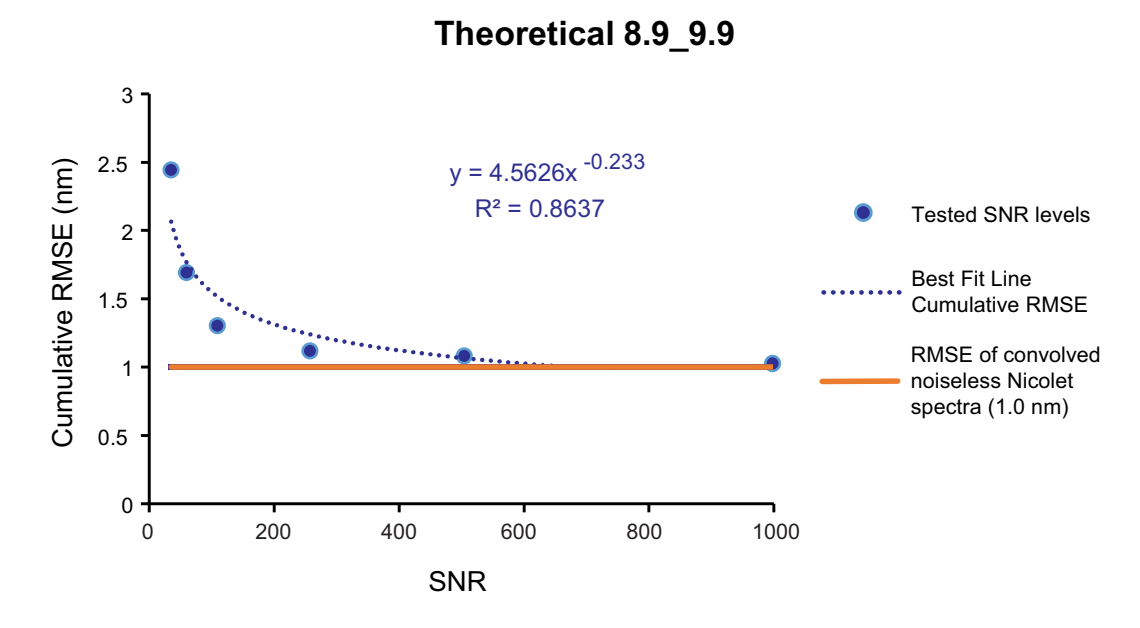


Fig. 12. Gaussian noise was added at SNR's of 25, 50, 100, 250, 500, and 1000 to 7500 Nicolet spectra convolved to the characteristics of the Theoretical 8.9_9.9 spectrometer. The position of the white mica 2200 nm combination feature in the noisy spectra was compared to the position in the convolved noiseless Nicolet spectra and the RMSE was determined for each SNR. The cumulative RMSE is the sum of the RMSE of the convolved noiseless Nicolet spectra, and the RMSE that results from the addition of noise.

white mica 2200 nm combination feature, a spectrometer with a sampling interval of 1 nm will record a smaller change in signal strength between channels centered on 2200 and 2201 nm than a spectrometer with a sampling interval of 10 nm will measure between channels centered on 2200 and 2210 nm. Small absolute fluctuations in signal strength due to noise will thus lead to larger relative changes in signal strength between channels in a fine spectrometer vs a coarse spectrometer. The likelihood of the position of an absorption feature, as determined using a quadratic best fit, shifting one channel due to noise is greater in a fine spectrometer with the characteristics of Theoretical

01_01 than it is in a coarse spectrometer with characteristics of Theoretical 8.9_9.9 due to the larger absolute difference in signal strength between adjacent channels in Theoretical 8.9_9.9. At a SNR of 25, it was determined that 5000 noisy spectra would be sufficient to produce robust results with spectrometer Theoretical 8.9_9.9 while 7500 noisy spectra would be required to produce robust results for Theoretical 01_01. Higher SNR levels required fewer noisy spectra in all spectrometers (see Table 2). Conducting testing with more samples than the minimum required will not affect the final results and, as was the case in this study, can streamline the testing process.

Table 4

Minimum Signal to Noise Ratios estimated to achieve cumulative RMSE's of 1, 1.5, and 2 nm when measuring noisy spectra using automatically adjusted endpoints as determined using the best fit equation. Cumulative RMSE comprises the RMSE in the measurement of the noiseless convolved spectra, and the RMSE in the measurement of the convolved noisy spectra. Note that the best fit equation line for the Theoretical 8.9_9.9 spectrometer deviates from the test data points in the 100 to 250 SNR range, thus estimates of RMSE calculated using SNR values in this range are less accurate.

Cumulative RMSE in noisy data (nm)	Theoretical 01_01 Required minimum SNR to achieve RMSE	Theoretical 05 Required minimum SNR to achieve RMSE	Theoretical 8.9_9.9 Required minimum SNR to achieve RMSE
1	245.9	430.6	Achieved with noiseless convolved Nicolet reference spectra
1.5	64	84.0	118.4
2	24.8	26.3	34.5

The techniques contained within the USGS PRISM software employed to measure the position of the white mica 2200 nm combination feature in this contribution were demonstrated to be fairly robust when applied to both noiseless and noisy spectral data. A calculation of the SNR required to produce results with RMSE of 1 and 2 nm indicates that accurate results can be achieved even with low SNR data. These results agree with previous studies that determined detection limits in noisy data (Swayze et al., 2003). The Theoretical 01_01 spectrometer, which has comparable characteristics to point spectrometers used in field and laboratory settings, requires a minimum SNR of 246 to achieve a RMSE of 1 nm in the measurement of the position of the white mica 2200 nm combination feature. A SNR of 246 is easily achievable in both the field and laboratory settings. Low SNR data collected with coarse spectrometers may also be used to accurately determine the position of the white mica 2200 nm combination feature. Data with a SNR of 35 collected using a spectrometer with the characteristics of the Theoretical 8.9 9.9 spectrometer would be expected to have a RMSE of 2 nm using adjusted continuum endpoints. High SNR in remotely sensed data may be obtained through image processing techniques such as pixel averaging (Kokaly et al., 2017b) and these techniques could be applied to coarse spectrometers in order to achieve a RMSE required for a particular study. Other methods can be applied to increase robustness of wavelength positions, including averaging multiple noisy channels to establish the continuum endpoints (Kokaly, 2011) and fitting larger order polynomials over a greater number of channels around the minimum in continuum-removed reflectance (Asadzadeh and de Souza Filho,

The use of theoretical spectrometers to model the expected performance of proposed spectrometers has been shown to be valid in this contribution. It is possible to effectively model spectrometer performance and to inform spectrometer design using theoretical spectrometers with easily varied characteristics. This reduces the need for time consuming testing involving measurements with real spectrometers built with varying characteristics, a costly endeavor.

7. Conclusions

The goal of this contribution was to conduct a review of spectral studies of white micas and to utilize information gleaned during the review to provide a guide to spectrometer design, specifically bandpass, sampling interval, channel position, and SNR. White micas were chosen as they are prevalent in many ore deposit types, with a known relationship between their chemistry and the position of the 2200 nm combination feature. Collectively, the review of spectral studies demonstrates that shifts as small as 1 nm in the position of the white mica 2200 nm combination feature may be geologically significant at a variety of deposit types. Thus, a RMSE of 1 nm in the determination of the

white mica 2200 nm combination feature was chosen as the baseline for the sensitivity study.

The initial sensitivity analysis utilized essentially noiseless spectra convolved from fine spectral resolution Nicolet reference spectra. It was determined that spectrometers with a sampling interval of $<\!8.8$ nm and a bandpass of $<\!9.8$ nm can determine the position of the white mica 2200 nm combination feature with a RMSE of 1 nm. Spectrometers with a sampling interval of $<\!16.3$ nm and a bandpass of $<\!17.6$ nm can determine the position of the white mica 2200 nm combination feature with a RMSE of 2 nm. Spectrometers with these characteristics are currently commercially available. Because all spectrometers have noise associated with the collected data, a second sensitivity analysis was then conducted to determine the effect of varying the SNR of the spectral data would have on the RMSE of the position determination of the white mica 2200 nm combination feature.

A SNR analysis determined that fine spectrometers, while the best performing spectrometers when SNR levels are high, are more affected by low SNR levels than coarse spectrometers. In a controlled laboratory setting where high SNR levels are easily obtainable, a fine spectrometer with characteristics comparable to the Theoretical 01_01 would be preferred. However, for outcrop, airborne, and orbital instruments, where an SNR in the 2200 nm region of 250 is typical, a coarser spectrometer with characteristics comparable to the Theoretical 05 will perform well. In situations where the SNR is 100 or less, a coarse spectrometer with characteristics comparable to the Theoretical 8.9_9.9 could be used if a particular study determined that a RMSE of 2 nm was adequate.

This contribution identified many areas of possible future work, related to both the white mica spectral studies review and the sensitivity analyses. Studies that quantitively linked ore grade and white mica 2200 nm combination feature position could be useful, both in a production setting and for near mine exploration projects. Studies similar to this one can be conducted on the spectral features of chlorites, smectites, and alunites, and their relationship to mineralized zones to aid in the development and refinement of geo-spectral deposit models. Sensitivity analyses such as conducted in this contribution can be performed on any spectrometer, proposed or existing.

Declaration of Competing Interest

The authors declare that they have no known competing financial interests or personal relationships that could have appeared to influence the work reported in this paper.

Acknowledgements

This project was funded by NSF EAR award # 1752756 (E. Holley) and in-kind support to J. Meyer from the U.S. Geological Survey (USGS) during an NSF-INTERN grant under the same award. We would like to acknowledge support provided for J. Meyer and R. Kokaly by the USGS National Land Imaging program's Sustainable Land Imaging hyperspectral imaging study (GX21ED00TYG1AAA) and the USGS Mineral Resources Program's hyperspectral imaging of mineral resources project (GX22RK00UGCX).

The authors thank Jason Rampe and Doug White of Newmont Corporation at the Cripple Creek & Victor Mine for allowing access to collect imaging spectroscopy data and for permission to publish images of their gold operation.

Finally, equipment and software support was provided through a volunteer for science opportunity at the USGS Spectroscopy Laboratory in Denver, Colorado. J. Meyer is extremely grateful for the time, assistance, and conversations provided by Todd Hoefen, Dr. Greg Swayze, Eric Livo, Dr. William Benzel, Dr. Karen Kelley, and Dr. Garth Graham of the USGS. Any use of trade, firm, or product names is for descriptive purposes only and does not imply endorsement by the U.S. Government.

Appendix A. Supplementary data

Supplementary data to this article can be found online at https://doi.org/10.1016/j.rse.2022.113000.

References

- Agus, A.J.L., 2011. Mapping white mica in milled porphyry copper pebbles using hyperspectral imagery: An exploratory study. In: Geo-Information Science and Earth, 57. University of Twente, Enschede, The Netherlands.
- Ahmed, A.D., Hickey, K.A., Barker, S.L., 2009. Tracing the distal hanging wall expression of Carlin-type hydrothermal. uids: A possible road-map to subsurface Au-deposits. In: Thermal and Geochemical Footprints of Low-Temperature Sedimentary Rock-Hosted Hydrothermal Au-Systems: Identifying Far-Field Vectors Toward Ore Year 2 Technical Summary. The University of British Columbia, Vancouver, British Columbia.
- Asadzadeh, S., de Souza Filho, C.R., 2016. Iterative curve fitting: a robust technique to estimate the wavelength position and depth of absorption features from spectral data. IEEE Trans. Geosci. Remote Sens. 54 (10), 5964–5974. https://doi.org/10.1109/TGRS.2016.2577621.
- Bakker, W., van Ruitenbeek, F., van der Werff, H., 2011. Hyperspectral Image Mapping by Automatic Color Coding of Absorption Features 7th EARSEL Workshop of the Special Interest Group in Imaging Spectroscopy: Final Programme Edinburgh, United Kingdom 56-57 11/04/11 to 13/04/11.
- Bierwirth, P., Huston, D., Blewett, R., 2002. Hyperspectral mapping of mineral assemblages associated with gold mineralization in the Central Pilbara, Western Australia. Econ. Geol. 97 (4), 819–826. https://doi.org/10.2113/gsecongeo.97.4.819.
- Bishop, J., Lane, M., Dyar, M., Brown, A., 2008. Reflectance and emission spectroscopy study of four groups of phyllosilicates: smectites, kaolinite-serpentines, chlorites and micas. Clay Miner. 43 (1), 35–54. https://doi.org/10.1180/claymin.2008.043.1.03.
- Cathelineau, M., 1988. Cation site occupancy in chlorites and illites as a function of temperature. Clay Miner. 23 (4), 471–485. https://doi.org/10.1180/claymin.1988.023.4.13.
- Clark, R.N., 1993. SPECtrum Processing Routines user's manual version 3 (program SPECPR). U.S. Geological Survey Open-File Report. https://pubs.er.usgs.gov/publication/ofr93595. https://doi.org/10.3133/ofr93595.
- Clark, R.N., 1999. Chapter 1. Spectroscopy of rocks and minerals, and principles of spectroscopy. In: Rencz, A.N. (Ed.), Manual of Remote Sensing, Volume 3, Remote Sensing for the Earth Sciences. John Wiley and Sons, Inc, New York, pp. 3–58.
- Clark, R.N., Roush, T.L., 1984. Reflectance spectroscopy: quantitative analysis techniques for remote sensing applications. J. Geophys. Res. 89 (B7), 6329–6340. https://doi.org/10.1029/JB089iB07p06329.
- Clark, R.N., King, T.V., Klejwa, M., Swayze, G.A., Vergo, N., 1990. High spectral resolution reflectance spectroscopy of minerals. J. Geophys. Res. Solid Earth 95 (B8), 12653–12680. https://doi.org/10.1029/JB095iB08p12653.
- Clark, Swayze, Livo, Kokaly, Sutley, Dalton, McDougal, Gent, 2003. Imaging spectroscopy: earth and planetary remote sensing with the USGS Tetracorder and expert systems. J. Geophys. Res. Planet 108 (E12). https://doi.org/10.1029/ 2002JE001847.
- Cline, J.S., Hofstra, A.H., Muntean, J.L., Tosdal, R.M., Hickey, K.A., 2005. Carlin-type gold deposits in Nevada: Critical geologic characteristics and viable models. In: Hedenquist, J.W., Thompson, J.F.H., Goldfarb, R.J., Richards, J.P. (Eds.), One Hundredth Anniversary Volume 484. Society of Economic Geologists. https://doi. org/10.5382/AV100.15.
- Cocks, T., Jenssen, R., Stewart, A., Wilson, I., Shields, T., 1998. The HyMapTM airborne hyperspectral sensor: The system, calibration and performance. In: Proceedings of the 1st EARSeL Workshop on Imaging Spectroscopy. EARSeL, Zurich, Switzerland, pp. 37–42.
- Cooke, D., Simmons, S., 2000. Characteristics and genesis of epithermal gold deposits. In: Gold in 2000. Society of Economic Geologists, pp. 221–244. https://doi.org/ 10.5382/Rev.13.
- Corescan Pty Ltd, 2019. The Corescan System. Accessed November, 2019. DOI: http://www.corescan.com.au/services/the-corescan-system.
- Dalm, M., Buxton, M., van Ruitenbeek, F., 2017. Discriminating ore and waste in a porphyry copper deposit using short-wavelength infrared (SWIR) hyperspectral imagery. Miner. Eng. 105, 10–18. https://doi.org/10.1016/j.mineng.2016.12.013.
- David, V., 2018. Cobar Deposits-Structural Control. ASEG Extended Abstracts, 2018, 1, pp. 1–10. https://doi.org/10.1071/ASEG2018abT6_2G.
- Duke, E.F., 1994. Near infrared spectra of muscovite, Tschermak substitution, and metamorphic reaction progress: implications for remote sensing. Geology 22 (7), 621–624. https://doi.org/10.1130/0091-7613(1994)022%3C0621:NISOMT% 3E2.3.C0-2.
- Duke, E.F., Lewis, R.S., 2010. Near infrared spectra of white mica in the belt supergroup and implications for metamorphism. Am. Mineral. 95 (7), 908–920. https://doi.org/ 10.2138/am.2010.3281.
- Farmer, V.C., 1974. Infrared spectra of minerals. Mineral. Soc. https://doi.org/10.1180/mono-4.
- Foster, M.D., 1956. Correlation of Dioctahedral Potassium Micas on the Basis of their Charge Relations, 1036. U.S. Government Printing Office Bulletin, pp. 56–67. https://doi.org/10.3133/b1036D.
- Franklin, J., Gibson, H., Jonasson, I., Galley, A., 2005. Volcanogenic massive sulfide deposits. In: Hedenquist, J.W., Thompson, J.F.H., Goldfarb, R.J., Richards, J.P.

- (Eds.), One Hundredth Anniversary Volume. Society of Economic Geologists, pp. 523–560. https://doi.org/10.5382/AV100.17.
- Goetz, A.F., Vane, G., Solomon, J.E., Rock, B.N., 1985. Imaging spectrometry for earth remote sensing. Science 228 (4704), 1147–1153. https://doi.org/10.1126/ science.228.4704.1147.
- Goldfarb, R., Baker, T., Dubé, B., Groves, D.I., Hart, C.J., Gosselin, P., 2005. Distribution, character and genesis of gold deposits in metamorphic terranes. In: Hedenquist, J. W., Thompson, J.F.H., Goldfarb, R.J., Richards, J.P. (Eds.), One Hundredth Anniversary Volume. Society of Economic Geologists. https://doi.org/10.5382/AVI00.14.
- Graham, G.E., Kokaly, R.F., Kelley, K.D., Hoefen, T.M., Johnson, M.R., Hubbard, B.E., 2018. Application of imaging spectroscopy for mineral exploration in Alaska: a study over porphyry cu deposits in the eastern Alaska range. Econ. Geol. 113 (2), 489–510. https://doi.org/10.5382/econgeo.2018.4559.
- Green, R.O., Eastwood, M.L., Sarture, C.M., Chrien, T.G., Aronsson, M., Chippendale, B. J., Faust, J.A., Pavri, B.E., Chovit, C.J., Solis, M., 1998. Imaging spectroscopy and the airborne visible/infrared imaging spectrometer (AVIRIS). Remote Sens. Environ. 65 (3), 227–248. https://doi.org/10.1016/S0034-4257(98)00064-9.
- Green, R.O., Mahowald, N.M., Clark, R.N., Ehlmann, B.L., Ginoux, P.A., Kalashnikova, O. V., Miller, R.L., Okin, G., Painter, T.H., Pérez García-Pando, C., 2018. NASA's earth surface mineral dust source investigation. In: American Geophysical Union, Fall Meeting 2018. American Geophysical Union.
- Gregory, M.J., Lang, J.R., Gilbert, S., Hoal, K.O., 2013. Geometallurgy of the pebble porphyry copper-gold-molybdenum deposit, Alaska: implications for gold distribution and paragenesis. Econ. Geol. 108 (3), 463–482. https://doi.org/10.2113/econgeo.108.3.463.
- Groves, D.I., Goldfarb, R.J., Gebre-Mariam, M., Hagemann, S., Robert, F., 1998. Orogenic gold deposits: a proposed classification in the context of their crustal distribution and relationship to other gold deposit types. Ore Geol. Rev. 13 (1–5), 7–27. https://doi.org/10.1016/S0169-1368(97)00012-7.
- Groves, D.I., Bierlein, F.P., Meinert, L.D., Hitzman, M.W., 2010. Iron oxide copper-gold (IOCG) deposits through earth history: implications for origin, lithospheric setting, and distinction from other epigenetic iron oxide deposits. Econ. Geol. 105 (3), 641–654. https://doi.org/10.2113/gsecongeo.105.3.641.
- Guilbert, J.M., Park Jr., C.F., 2007. The Geology of Ore Deposits. Waveland Press, Long Grove, IL. https://doi.org/10.1007/BF01041818.
- Guo, N., Thomas, C., Tang, J., Tong, Q., 2019. Mapping white mica alteration associated with the Jiama porphyry-skarn Cu deposit, central Tibet using field SWIR spectrometry. Ore Geol. Rev. 108, 11. https://doi.org/10.1016/j. oregeorev.2017.07.027.
- Hamlin, L., Green, R., Mouroulis, P., Eastwood, M., Wilson, D., Dudik, M., Paine, C., 2011. Imaging spectrometer science measurements for terrestrial ecology: AVIRIS and new developments. In: 2011 Aerospace Conference. IEEE, Big Sky, Montana, USA, pp. 1–7. https://doi.org/10.1109/AERO.2011.5747395.
- Harraden, C.L., Mcnulty, B.A., Gregory, M.J., Lang, J.R., 2013. Shortwave infrared spectral analysis of hydrothermal alteration associated with the pebble porphyry copper-gold-molybdenum deposit, Iliamna, Alaska. Econ. Geol. 108 (3), 483–494. https://doi.org/10.2113/econgeo.108.3.483.
- Harris, D.C., Bertolucci, M.D., 1989. Symmetry and Spectroscopy: An Introduction to Vibrational and Electronic Spectroscopy. Dover Publications, Inc, New York, New York
- Hedenquist, J.W., Arribas, A., Gonzalez-Urien, E., 2000. Exploration for epithermal gold deposits. In: Hagemann, S.G., Brown, P.E. (Eds.), Gold in 2000. Society of Economic Geologists, pp. 245–277. https://doi.org/10.5382/Rev.13.07.
- Herrmann, W., Blake, M., Doyle, M., Huston, D., Kamprad, J., Merry, N., Pontual, S., 2001. Short wavelength infrared (SWIR) spectral analysis of hydrothermal alteration zones associated with base metal sulfide deposits at Rosebery and Western Tharsis, Tasmania, and highway-reward, Queensland. Econ. Geol. 96 (5), 939–954. https://doi.org/10.2113/96.5.939
- Hewson, R., Cudahy, T., Mizuhiko, S., Ueda, K., Mauger, A., 2005. Seamless geological map generation using ASTER in the Broken Hill-Curnamona province of Australia. Remote Sens. Environ. 99 (1–2), 159–172. https://doi.org/10.1016/j. rse.2005.04.025.
- Hitzman, M.W., Oreskes, N., Einaudi, M.T., 1992. Geological characteristics and tectonic setting of proterozoic iron oxide (Cu-U-Au-REE) deposits. Precambrian Res. 58 (1–4), 241–287. https://doi.org/10.1016/0301-9268(92)90121-4.
- Huang, J., Chen, H., Han, J., Deng, X., Lu, W., Zhu, R., 2018. Alteration zonation and short wavelength infrared (SWIR) characteristics of the Honghai VMS Cu-Zn deposit, Eastern Tianshan, NW China. Ore Geol. Rev. 100, 263–279. https://doi.org/ 10.1016/j.oregeorev.2017.02.037.
- Hubbard, B.E., Crowley, J.K., Zimbelman, D.R., 2003. Comparative alteration mineral mapping using visible to shortwave infrared (0.4-2.4 μm) Hyperion, ALI, and ASTER imagery. IEEE Trans. Geosci. Remote Sens. 41 (6), 1401–1410. https://doi.org/ 10.1109/TGRS.2003.812906
- Hunt, G.R., 1977. Spectral signatures of particulate minerals in the visible and near infrared. Geophysics 42 (3), 501–513. https://doi.org/10.1190/1.1440721.
- Hunt, G., Ashley, R., 1979. Spectra of altered rocks in the visible and near infrared. Econ. Geol. 74 (7), 1613–1630. https://doi.org/10.2113/gsecongeo.74.7.1613.
- Huston, D.L., Blewett, R.S., Keillor, B., Standing, J., Smithies, R.H., Marshall, A., Mernagh, T.P., Kamprad, J., 2002. Lode gold and epithermal deposits of the Mallina basin, North Pilbara terrain, Western Australia. Econ. Geol. 97 (4), 801–818. https:// doi.org/10.2113/gsecongeo.97.4.801.
- Jefferson, C., Thomas, D., Gandhi, S., Ramaekers, P., Delaney, G., Brisbin, D., Cutts, C., Portella, P., Olson, R., 2007. Unconformity-associated uranium deposits of the Athabasca Basin, Saskatchewan and Alberta. In: Jefferson, C.W., Delaney, G. (Eds.),

- Bulletin of the Geological Survey of Canada. Natural Resources Canada, pp. 23–67. https://doi.org/10.4095/223744.
- Jones, S., Herrmann, W., Gemmell, J.B., 2005. Short wavelength infrared spectral characteristics of the HW horizon: implications for exploration in the Myra Falls volcanic-hosted massive sulfide camp, Vancouver Island, British Columbia, Canada. Econ. Geol. 100 (2), 273–294. https://doi.org/10.2113/gsecongeo.100.2.273.
- Klein, C., Dutrow, B., Dana, J.D., 2007. The 23rd Edition of the Manual of Mineral Science:(after James D. Dana). John Wiley & Sons, New York, New York.
- Kokaly, R., 2011. PRISM: Processing routines in IDL for spectroscopic measurements (installation manual and user's guide, version 1.0). In: U.S.Geological Survey Open-File Report 2011–1155. https://doi.org/10.3133/ofr20111155.
- Kokaly, R.F., Turpie, K.R., 2019. Calibration and validation working group for surface biology and geology (SBG). In: IGARSS 2019–2019 IEEE International Geoscience and Remote Sensing Symposium. IEEE, Yokohama, Japan, pp. 8517–8518. https:// doi.org/10.1109/IGARSS.2019.8900236.
- Kokaly, R., King, T., Hoefen, T., 2013. Surface Mineral Maps of Afghanistan Derived from HyMap Imaging Spectrometer Data, Version 2: US Geological Survey Data Series, 787. U.S. Geological Survey Data Series. https://doi.org/10.3133/ds787, 29 p.
- Kokaly, R.F., Clark, R.N., Swayze, G.A., Livo, K.E., Hoefen, T.M., Pearson, N.C., Wise, R. A., Benzel, W.M., Lowers, H.A., Driscoll, R.L., 2017a. USGS Spectral Library Version 7, 1035. US Geological Survey Data Series, p. 61. https://doi.org/10.3133/ds1035.
- Kokaly, R.F., Graham, G.E., Hoefen, T.M., Kelley, K.D., Johnson, M.R., Hubbard, B.E., Buchhorn, M., Prakash, A., 2017b. Multiscale hyperspectral imaging of the Orange Hill porphyry copper deposit. In: Proceedings of Exploration 17: Sixth Decennial International Conference on Mineral Exploration. Decennial Mineral Exploration Conferences, pp. 923–943.
- Kokaly, R.F., Swayze, G.A., Livo, K.E., Hoefen, T.M., Hubbard, B.E., Meyer, J.M., Cox, E. M., Gnesda, W.R., 2021. Imaging spectroscopy applied to mineral mapping over large areas: Impact of residual atmospheric artefacts in reflectance spectra on mineral identification and mapping. In: 2021 IEEE International Geoscience and Remote Sensing Symposium IGARSS. IEEE, pp. 1855–1858. https://doi.org/10.1109/IGARSS47720.2021.9553752.
- Kruse, F.A., Bedell, R.L., Taranik, J.V., Peppin, W.A., Weatherbee, O., Calvin, W.M., 2012. Mapping alteration minerals at prospect, outcrop and drill core scales using imaging spectrometry. Int. J. Remote Sens. 33 (6), 1780–1798.
- Laakso, K., Peter, J., Rivard, B., White, H., 2016. Short-wave infrared spectral and geochemical characteristics of hydrothermal alteration at the Archean Izok Lake Zn-Cu-Pb-Ag volcanogenic massive sulfide deposit, Nunavut, Canada: application in exploration target vectoring. Econ. Geol. 111 (5), 1223–1239. https://doi.org/ 10.2113/econgeo.111.5.1223.
- Lang, J.R., Gregory, M.J., Rebagliati, C.M., Payne, J.G., Oliver, J.L., Roberts, K., 2013. Geology and magmatic-hydrothermal evolution of the giant pebble porphyry copper-gold-molybdenum deposit, Southwest Alaska. Econ. Geol. 108 (3), 437–462. https://doi.org/10.2113/econgeo.108.3.437.
- Lawrie, K., Hinman, M., 1998. Cobar-style polymetallic Au-Cu-Ag-Pb-Zn deposits. AGSO J. Aust. Geol. Geophys. 17 (4), 169–187.
- Liang, S., Li, X., Wang, J., 2019. Advanced Remote Sensing: Terrestrial Information Extraction and Applications, 2 ed. Academic Press. https://doi.org/10.1016/B978-0-12-815826-5-01001-1
- Lypaczewski, P., Rivard, B., Gaillard, N., Perrouty, S., Piette-Lauzière, N., Bérubé, C.L., Linnen, R.L., 2019. Using hyperspectral imaging to vector towards mineralization at the Canadian Malartic gold deposit, Québec, Canada. Ore Geol. Rev. 111, 15. https://doi.org/10.1016/j.orgegorgy.2019.102945
- https://doi.org/10.1016/j.oregeorev.2019.102945.

 Malvern Panalytical, 2018a. ASD FieldSpec® 4 Hi-Res NG Spectroradiometer. accessed December, 2018,. https://www.malvernpanalytical.com/en/products/product-range/asd-range/fieldspec-range/fieldspec-4-hi-res-ng-spectroradiometer/.
- Malvern Panalytical, 2018b. ASD FieldSpec®Full-range. accessed December, 2018. https://www.malvernpanalytical.com/en/products/product-range/asd-range/fieldspec-range/index.html.
- Martínez-Alonso, S., Rustad, J.R., Goetz, A.F., 2002. Ab initio quantum mechanical modeling of infrared vibrational frequencies of the OH group in dioctahedral phyllosilicates. Part II: main physical factors governing the OH vibrations. Am. Mineral. 87 (8–9), 1224–1234. https://doi.org/10.2138/am-2002-8-922.
- Mateer, M.A., 2010. Ammonium illite at the Jerritt Canyon district and Goldstrike property, Nevada: Its spatial distribution and significance in the exploration of Carlin-type deposits. In: Geology and Geophysics, 214. University of Wyoming.
- Mathieu, M., Roy, R., Launeau, P., Cathelineau, M., Quirt, D., 2017. Alteration mapping on drill cores using a HySpex SWIR-320m hyperspectral camera: application to the exploration of an unconformity-related uranium deposit (Saskatchewan, Canada). J. Geochem. Explor. 172, 71–88. https://doi.org/10.1016/j.gexplo.2016.09.008.
- Meyer, J.M., Kokaly, R., Hoefen, T.M., Graham, G.E., Kelley, K.D., 2022. HySpex VNIR-1800 and SWIR-384 Imaging Spectrometer Radiance and Reflectance Data, with Associated ASD FieldSpec NG Calibration Data, Collected at Cripple Creek Victor Mine, Cripple Creek, Colorado, 2017. U.S. Geological Survey data release. https://doi.org/10.5066/P92VF8HP.
- Nicolet Instrument Corporation, 1997. Magna-IR FTIR Spectrometers System 560 and 760 User's Guide. accessed June, 2020. DOI: http://nano.ee.uh.edu/Text/Nicolet% 20Magna-IR%20560%20Manual.pdf.
- Norsk Elektro Optikk AS, 2016. HySpex SWIR-384. accessed June, 2017, http://www.hyspex.no/products/.
- Parry, W.T., Ballantyne, J.M., Jacobs, D.C., 1984. Geochemistry of hydrothermal sericite from Roosevelt Hot Springs and the Tintic and Santa Rita porphyry copper systems. Econ. Geol. 79 (1), 72–86. https://doi.org/10.2113/gsecongeo.79.1.72.
- Pearlman, J.S., Barry, P.S., Segal, C.C., Shepanski, J., Beiso, D., Carman, S.L., 2003. Hyperion, a space-based imaging spectrometer. IEEE Trans. Geosci. Remote Sens. 41 (6), 1160–1173. https://doi.org/10.1109/TGRS.2003.815018.

- Post, J.L., Noble, P.N., 1993. The near-infrared combination band frequencies of dioctahedral smectites, micas, and illites. Clay Clay Miner. 41, 639–640. https://doi. org/10.1346/CCMN.1993.0410601.
- Richter, R., Schläpfer, D., 2019. ATCOR-4 User Guide, Version 7.3. 0, Atmospheric/ Topographic Correction for Airborne Imagery. accessed July, 2020. https://www.rese-apps.com/pdf/atcor4_manual.pdf.
- Rieder, M., Cavazzini, G., D'yakonov, Y.S., Frank-Kamenetskii, V.A., Gottardi, G., Guggenheim, S., Koval, P.V., Mueller, G., Neiva, A.M., Radoslovich, E.W., 1998. Nomenclature of the micas. Clay Clay Miner. 46 (5), 586–591. https://doi.org/ 10.1180/002646199548385.
- Robb, L., 2004. Introduction to Ore-Forming Processes. Blackwell Publishing, Oxforn, UK. https://doi.org/10.2138/am.2005.426.
- Rossman, G.R., 1984. Spectroscopy of micas. In: Bailey, S.W. (Ed.), Micas, pp. 145–182. https://doi.org/10.1515/9781501508820-009.
- Sang, B., Schubert, J., Kaiser, S., Mogulsky, V., Neumann, C., Förster, K.-P., Hofer, S., Stuffler, T., Kaufmann, H., Müller, A., 2008. The EnMAP hyperspectral imaging spectrometer: Instrument concept, calibration, and technologies. In: Optical Engineering + Applications. International Society for Optics and Photonics, San Diego, California. https://doi.org/10.1117/12.794870.
- Seedorff, E., Dilles, J.H., John M. Proffett, J., Einaudi, M.T., Zurcher, L., Stavast, W.J.A., Johnson, D.A., Barton, M.D., 2005. Porphyry deposits: Characteristics and origin of hypogene features. In: Hedenquist, J.W., Thompson, J.F.H., Goldfarb, R.J., Richards, J.P. (Eds.), One Hundredth Anniversary Volume. Society of Economic Geologists, pp. 251–298. https://doi.org/10.5382/AV100.10.
- Shanks III, W.C.P., Koski, R.A., Mosier, D.L., Schulz, K.J., Morgan, L.A., Slack, J.F., Ridley, W.I., Dusel-Bacon II, C., Piatak, N.M., 2012. Volcanogenic massive sulfide occurrence model: Chapter C in Mineral deposit models for resource assessment. In: U.S. Geological Survey Scientific Investigations Report 2010-5070, p. 345. https:// doi.org/10.3133/sir20105070C.
- Sillitoe, R.H., 2010. Porphyry copper systems. Econ. Geol. 105 (1), 3–41. https://doi.org/10.2113/gsecongeo.105.1.3.
- Simmons, S.F., White, N.C., John, D.A., 2005. Geological characteristics of epithermal precious and base metal deposits. In: Hedenquist, J.W., Thompson, J.F.H., Goldfarb, R.J., Richards, J.P. (Eds.), One Hundredth Anniversary Volume. Society of Economic Geologists, pp. 485–522. https://doi.org/10.5382/AV100.16.
- SpecTIR Inc, 2018. Featured Instruments. accessed July, 2019. https://www.spectir.com/technology#featured-instruments.
- Spectral Evolution Inc, 2019. Product. accessed 2019. https://spectralevolution.com/products/.
- Squire, R.J., Herrmann, W., Pape, D., Chalmers, D.I., 2007. Evolution of the Peak Hill high-sulfidation epithermal Au–Cu deposit, Eastern Australia. Mineral. Deposita 42 (5), 489–503. https://doi.org/10.1007/s00126-006-0076-4.
- Sun, Y., Seccombe, P.K., Yang, K., 2001. Application of short-wave infrared spectroscopy to define alteration zones associated with the Elura zinc-lead-silver deposit, NSW, Australia. J. Geochem. Explor. 73 (1), 11–26. https://doi.org/10.1016/S0375-6742 (01)00167-4.
- Swayze, G., Clark, R.N., Kruse, F., Sutley, S., Gallagher, A., 1992. Ground-truthing AVIRIS mineral mapping at Cuprite, Nevada. In: National Aeronautics and Space Administration, Jet Propulsion Laboratory, California Institute of Technology NASA contractor report NASA CR-194540. 194541. 194542.
- Swayze, G.A., Clark, R.N., Goetz, A.F., Chrien, T.G., Gorelick, N.S., 2003. Effects of spectrometer band pass, sampling, and signal-to-noise ratio on spectral identification using the Tetracorder algorithm. J. Geophys. Res. Planet 108 (E9), 1–31. https://doi. org/10.1029/2002.JE001975.
- Swayze, G.A., Clark, R.N., Goetz, A.F., Livo, K.E., Breit, G.N., Kruse, F.A., Sutley, S.J., Snee, L.W., Lowers, H.A., Post, J.L., Stoffregen, R.E., Ashley, R.P., 2014. Mapping advanced argillic alteration at cuprite, Nevada, using imaging spectroscopy. Econ. Geol. 109 (5), 1179–1222. https://doi.org/10.2113/econgeo.109.5.1179.
- Tappert, M., Rivard, B., Giles, D., Tappert, R., Mauger, A., 2011. Automated drill core logging using visible and near-infrared reflectance spectroscopy: a case study from the Olympic Dam IOCG deposit, South Australia. Econ. Geol. 106 (2), 289–296. https://doi.org/10.2113/econgeo.106.2.289.
- ThermoFisher Scientific, 2019. Nicolet FTIR Instruments. accessed November, 2019. htt ps://www.thermofisher.com/us/en/home/industrial/spectroscopy-elemental-isoto pe-analysis/molecular-spectroscopy/fourier-transform-infrared-ftir-spectroscopy/ftir-instruments.html.
- Thompson, D.R., Babu, K., Braverman, A.J., Eastwood, M.L., Green, R.O., Hobbs, J.M., Jewell, J.B., Kindel, B., Massie, S., Mishra, M., 2019. Optimal estimation of spectral surface reflectance in challenging atmospheres. Remote Sens. Environ. 232, 111258 https://doi.org/10.1016/j.rse.2019.111258.
- Uribe-Mogollon, C., Maher, K., 2018. White mica geochemistry of the copper cliff porphyry Cu deposit: insights from a vectoring tool applied to exploration. Econ. Geol. 113 (6), 1269–1295. https://doi.org/10.5382/econgeo.2018.4591.
- Uribe-Mogollon, C., Maher, K., 2020. White mica geochemistry: discriminating between barren and mineralized porphyry systems. Econ. Geol. 115 (2), 325–354. https:// doi.org/10.5382/econgeo.4706.
- van der Meer, F.D., van der Werff, H.M., van Ruitenbeek, F.J., Hecker, C.A., Bakker, W. H., Noomen, M.F., van der Meijde, M., Carranza, E.J.M., de Smeth, J.B., Woldai, T., 2012. Multi-and hyperspectral geologic remote sensing: a review. Int. J. Appl. Earth Obs. Geoinf. 14 (1), 112–128. https://doi.org/10.1016/j.jag.2011.08.002.
- van Ruitenbeek, F.J., Cudahy, T., Hale, M., van der Meer, F.D., 2005. Tracing fluid pathways in fossil hydrothermal systems with near-infrared spectroscopy. Geology 33 (7), 597–600. https://doi.org/10.1130/G21375.1.
- van Ruitenbeek, F.J., Bakker, W.H., van der Werff, H.M., Zegers, T.E., Oosthoek, J.H., Omer, Z.A., Marsh, S.H., van der Meer, F.D., 2014. Mapping the wavelength position

of deepest absorption features to explore mineral diversity in hyperspectral images. Planet. Space Sci. 101, 108–117. https://doi.org/10.1016/j.pss.2014.06.009.

Vedder, W., 1964. Correlations between infrared spectrum and chemical composition of mica. Am. Mineral. 49 (5–6), 736–768.

Wedepohl, H., 1986. Chapter 5: the composition of the continental crust. Int. Geophys. 213–241.

Yang, K., Huntington, J., Boardman, J., Mason, P., 1999. Mapping hydrothermal alteration in the Comstock mining district, Nevada, using simulated satellite-borne

hyperspectral data. Aust. J. Earth Sci. 46 (6), 915–922. https://doi.org/10.1046/j.1440-0952.1999.00754.x.

Yang, K., Huntington, J., Gemmell, J., Scott, K., 2011. Variations in composition and abundance of white mica in the hydrothermal alteration system at Hellyer, Tasmania, as revealed by infrared reflectance spectroscopy. J. Geochem. Explor. 108 (2), 143–156. https://doi.org/10.1016/j.gexplo.2011.01.001.